Tampere University

Huseyin Babaroglu

RECEIVER SIDE SIGNAL PROCESSING FOR NONLINEAR DISTORTION COMPENSATION IN 5G AND BEYOND

Master of Science Thesis
Faculty of Information Technology and Communication Sciences
Examiners: Prof. Mikko Valkama
Dr. Guixian Xu
April 2023

ABSTRACT

Huseyin Babaroglu: Receiver Side Signal Processing for Nonlinear Distortion Compensation in 5G AND Beyond
Master of Science Thesis
Tampere University
Master's Degree Programme in Electrical Engineering
April 2023

Trading between transmit waveform quality and power efficiency is one of the most challenging issues in radio transmitter implementation. To this end, digital predistortion is the de-facto solution for mitigating power amplifier (PA) nonlinear distortion in cellular base-stations due to its high flexibility and good linearization performance. Theoretically, it is convenient to describe predistorter (PD) transfer function as the mathematical inverse of the PA transfer function, and PD modeling is often performed through parametric methods. Thus, an additional feedback loop is required in the system for PD model parameter estimation. PA is an analog device and DPD is a part of digital front-end, implying that PA output signal is needed to be downconverted to baseband and sampled in the parameter estimation path. Consequently, it is required to employ additional components in the feedback loop such as attenuator, downconverter, and analog-to-digital converter (ADC). In order to be able to capture higher order nonlinearities, it is necessary to perform upsampling operation, which implies that in addition to digital-to-analog converters (DACs) in the forward loop, the components in the feedback loop should support higher bandwidths than the original transmission bandwidth. Additionally, to have a good linearization performance, a high resolution ADC is required. Having an ADC/DAC that supports wide bandwidth and has high resolution is directly increasing the material cost and power consumption. When future millimeter-wave (mmWave) systems are considered, adopting DPD becomes even more complex and costly due to wider waveform bandwidths and employing active antenna arrays.

Alternative to DPD, receiver based approaches, referred to as digital post-distortion (DPoD), can be utilized to mitigate the nonlinear effects of transmitter PA. Naturally, receiver side techniques do not provide any improvement in terms of out-of-band (OOB) emission issues, rather they aim to improve received signal error vector magnitude (EVM). As the radiated power at mmWave is typically EVM limited and OOB emission requirements are relaxed compared to sub-6 GHz band, DPoD can offer means for improved network energy-efficiency. Several iterative DPoD methods are proposed in the literature such as power amplifier nonlinearity cancellation (PANC), and reconstruction of distorted signals (RODS). In this thesis, we present a non-iterative computationally efficient receiver side nonlinearity mitigation technique, referred to as digital post-inverse (DPoI), along with the parameter estimation approach targeting existing 5G NR standard-compliant reference signal. The receiver EVM performance of presented approach is analyzed by using computer simulations. It is seen that DPoI can reach similar or improved performance compared to the iterative PANC method, which is chosen as a reference DPoD method. Moreover, it is shown that both DPoD methods overperform ideally linearized transmitter PA under strong nonlinear conditions, which allows higher power efficiency when receiver side techniques are employed.

Keywords: 5G, 6G, active array, digital post-distortion, energy efficiency, nonlinear distortion, power amplifiers, behavioral modeling

PREFACE

The work presented in this Master of Science thesis was written at the Department of Electrical Engineering at Tampere University, and is a part of *Energy-Efficient Radio Systems at 100 GHz and Beyond: Antennas, Transceivers and Waveforms (ENTRY100GHz)* project.

First and foremost, Dr. Lauri Anttila and Prof. Mikko Valkama, throughout the development of this thesis, have been extraordinary guides and advisors to me. I am truly grateful for their guidance, insightful advice, and giving me the opportunity to work in their research group.

My biggest thanks and gratitude, of course, goes to my parents, Numan and Tuba Babaroglu, my little sister, Duygu Babaroglu, and to my beloved wife, my best friend, Safak Babaroglu, for always supporting and believing in me, not only during my M.Sc. studies, but also throughout my whole life. You are the pillars of everything I achieved and I am going to achieve.

Tampere, 18th April 2023

Huseyin Babaroglu

CONTENTS

LIST OF FIGURES

LIST OF TABLES

LIST OF SYMBOLS AND ABBREVIATIONS

$A(t)$	Instantaneous envelope of the power amplifier input signal
G	Power gain of a power amplifier
G_{dB}	Power gain of a power amplifier in decibels
N_{CP}	Cyclix prefix length
N_{FFT}	FFT size
N_{act}	Number of active subcarriers
$P_{\text{1-dB}}$	1-dB compression point
P_{DC}	Power amplifier DC supply power
P_{RX}	Memory depth of post-distortion model
P_{RX}	Nonlinearity order of post-distortion model
P_{TX}	Memory depth of nonlinear transmitter model
P_{TX}	Nonlinearity order of nonlinear transmitter model
$P_{\text{in,avg}}$	Average power of power amplifier input signal
$P_{\text{in,sat}}$	Power amplifier input saturation power
P_{in}	Power amplifier input power
P_{out}	Power amplifier output power
T_c	NR basic time unit
T_{sym}	OFDM symbol duration
W	Transmission bandwidth
Δf	Subcarrier spacing
$\tilde{c}_{p,d}$	Complex coefficient of p-th order and d-th delayed nonlinearity of the inverse nonlinear model
$\Upsilon_{p,d}$	Basis function of p-th order and d-th delayed nonlinearity
α_a, β_a, α_p, β_p	Saleh model fitting parameters
$\tilde{\boldsymbol{c}}$	Vector of inverse nonlinear complex coefficients
$\boldsymbol{\Upsilon}$	Basis function matrix
$\underline{\underline{K}}^{(m)}$	Relation matrix between original and distorted symbols in RODS algorithm

η	Power amplifier drain efficiency
η_{PAE}	Power amplifier power added efficiency
γ	Instantaneous power of the signal in RODS algorithm
$\hat{x}(n)$	Discrete time estimation of the power amplifier input signal
$\mathbf{D}(\mathbf{k})$	DFT/FFT of $d(n)$
$\mathbf{E}(.)$	Expected value operator
$\mathbf{H}(\mathbf{k})$	DFT/FFT of $h(n)$
$\mathbf{H}_{\text{est}}$	Estimated channel frequency response
$\mathbf{Q}(\mathbf{k})$	DFT/FFT of $q(n)$
$\mathbf{W}(\mathbf{k})$	DFT/FFT of $w(n)$
$\mathbf{X}(\mathbf{k})$	DFT/FFT of $x(n)$
μ	Subcarrier spacing configuration
ω	Frequency unit in radians
ω_c	Center frequency in radians
$\phi(t)$	Instantaneous phase of the power amplifier input signal
ε	Upsampling/downsampling factor
a_k	Modulation symbols
$c_{p,d}$	Complex coefficient of p-th order and d-th delayed nonlinearity of a power amplifier behavioural model
$d(n)$	Discrete time nonlinear distortion term in PANC algorithm
f	Frequency variable in Hertz
$f(.)$	Nonlinear function
$f_A(.)$	Power amplifier AM/AM conversion function
$f_D(.)$	Non-recursive nonlinear function with memory
$f_P(.)$	Power amplifier AM/PM conversion function
$f_R(.)$	Recursive nonlinear function with memory
$f_a(.)$	Saleh model AM/AM conversion function
$f_p(.)$	Saleh model AM/PM conversion function
$h(n)$	Discrete time finite impulse response of the channel
$h_p(.)$	Volterra kernel
k	Subcarrier index relative to a reference
l	OFDM symbol index relative to a reference

n	Discrete time index
$q(n)$	Discrete time signal at LMMSE equalizer output
$q_{ref}(n)$	Reference signal at LMMSE equalizer output
$r(n)$	Discrete time received signal
t	Continuous time variable
$u_H(n)$	Hammerstein model intermediate signal
$u_W(n)$	Wiener model intermediate signal
$w(n)$	Discrete time additive white Gaussian noise
$x(n)$	Discrete time OFDM symbol
$x(t)$	Continuous time OFDM symbol
$x_{RF}(t)$	Passband equivalent of power amplifier input signal
$x_{ref}(n)$	Discrete time reference power amplifier input signal
$y(n)$	Discrete time PA output signal
$y(t)$	Continuous time PA output signal
$y_H(n)$	Hammerstein model output signal
$y_W(n)$	Wiener model output signal
$y_{RF}(t)$	Passband equivalent of power amplifier output signal
$y_{WH}(n)$	Wiener-Hammerstein model output signal
5G NR	Fifth Generation New Radio
ACLR	adjacent channel leakage ratio
ADC	analog-to-digital converter
AM/AM	amplitude to amplitude mapping
AM/PM	amplitude to phase mapping
ANN	artificial neural network
APD	analog pre-distortion
AWGN	additive white Gaussian noise
BWP	bandwidth part
CP	cyclic prefix
CRB	common resource block
CSI	channel-state information
CSI-RS	channel-state information reference signal
DAC	digital-to-analog converter

DC	direct current
DE	drain efficiency
DFT	discrete Fourier transform
DM-RS	demodulation reference signal
DPD	digital pre-distortion
DPoD	digital post-distortion
DPoI	Digital Post-Inverse
eMBB	enhanced mobile broadband
EVM	error vector magnitude
FFT	fast Fourier transform
FIR	finite impulse response
FR1	frequency range 1
FR2	frequency range 2
GMP	generalized memory polynomial
IBO	input back-off
IDFT	inverse discrete Fourier transform
IFFT	inverse fast Fourier transform
ISI	inter symbol interference
LMMSE	linear minimum mean squared error
LTE	long term evolution
MAC	media access control
MIMO	multiple input multiple output
mIoT	massive Internet of Things
mmWave	millimeter-wave
MP	memory polynomial
MU-MIMO	multi-user MIMO
OFDM	orthogonal frequency division multiplexing
OOB	out-of-band
PA	power amplifier
PAE	power added efficiency
PANC	power amplifier nonlinearity cancellation
PAPR	peak-to-average power ratio

PBCH	physical broadcast channel
PD	predistorter
PDCCH	physical downlink control channel
PDSCH	physical downlink shared channel
PRB	physical resource block
PRS	positioning reference signal
PT-RS	phase-tracking reference signal
PUCCH	physical uplink control channel
PUSCH	physical uplink shared channel
QAM	quadrature amplitude modulation
QPSK	quadrature phase shift keying
RF	radio frequency
RIM-RS	remote interference management reference signal
RMS	root mean square
RODS	recounstruction of distorted signals
SEL	soft envelope limiter
SFN	system frame number
SISO	single input single output
SNR	signal-to-noise ratio
SRS	sounding reference signal
TDL	tapped delay line
TRS	tracking reference signal
TWT	travelling-wave tube
UE	user equipment
URLLC	ultra reliable and low latency communications

1. INTRODUCTION

Over the last decade, the enormous increase in the number of wireless devices along with the increasing demand for higher data rates has led to the development of modern communication systems. Fifth Generation New Radio (5G NR) is designed to satisfy this demand in mobile communication industry, also addressing the new services and markets such as enhanced mobile broadband (eMBB), ultra reliable and low latency communications (URLLC), massive Internet of Things (mIoT), and flexible network operations. Based on the application, each of the use cases discussed above has a different priority for system level design requirements, such as coverage, number of supported connections, mobility, latency, throughput, and battery life. Satisfying such system level design requirements imposes strict limitations to the different elements of a wireless system, standardized by regulatory bodies. Throughout the thesis, we mainly focus on transceiver related design requirements.

Any modern communication transceiver, generally speaking, includes both digital signal processing and analog signal processing. Digital signal processing part of a transceiver includes all baseband operations such as modulation/demodulation, coding/decoding, interleaving/deinterleaving etc. whereas analog signal processing part is mainly consisted of antenna arrays, mixers, filters, amplifiers, amplifiers and includes operations associated with these elements [1]; and the mapping between these two domains is handled by analog-to-digital converters (ADC) and digital-to-analog converters (DAC).

Power amplifiers (PA), as a part of analog RF front-end, play a crucial role in any wireless transmitter by being in charge of boosting the transmit waveform to a certain level before propagating through wireless media such that reliable detection is possible at the receiver. It is often the most power consuming element of a transmitter that dominates the overall transmitter power efficiency, making amplifier power efficiency a key parameter in transceiver design. To this end, it is required to operate PA at its highest output power, close to saturation, where it is more energy efficient [2]. However, operating close to saturation also causes PA to have a strong nonlinear behaviour, introducing in-band distortion and out-of-band spectral emission. The in-band distortion and out-of-band (OOB) emission which are characterized by error vector magnitude (EVM) and adjacent channel leakage ratio (ACLR), respectively, should be kept within certain limits to meet the specifications mandated by the regulatory and standardization bodies. The detrimental

effects of a nonlinear PA are more severe when modulation schemes with high peak-to-average power ratio (PAPR) such as orthogonal frequency division multiplexing (OFDM) are used. It is practically very challenging to achieve both energy efficient and highly linear PA simultaneously [3], thus it is essential to apply linearization techniques.

There are various approaches to combat with the detrimental effects of nonlinear PA in the literature. Among others, digital pre-distortion (DPD) has become very popular and preferred in modern wireless communication systems due its high flexibility and good linearization performance [4]. The basic idea of DPD is placing a nonlinear structure before PA such that their combined response allows a linear amplification of the original input signal. Although DPD has been widely used in modern wireless communication systems, future millimeter-wave (mmWave) systems with wide bandwidths and active antenna arrays with high number of elements make adopting DPD increasingly complex and costly [3]. As an alternative approach to DPD, detrimental effects of nonlinear PA can be mitigated with the structures employed at the receiver side, referred to as digital post-distortion (DPoD) [5]. Naturally, DPoD techniques do not provide any improvement in terms of unwanted transmitter out-of-band emissions, rather they primarily target to enhance the received signal EVM. However, as the radiated power at the mmWaves is typically EVM limited [6], DPoD can be considered as a promising approach to be used in the current and future mmWave wireless communication systems. To this end, DPoD methods can have wide applications already along the evolution of the 5G networks. Additionally, the energy efficiency and sustainability requirements are expected to be of even bigger importance in the future 6G era, hence, developing cellular DPoD techniques is part of a forward looking research agenda towards the next generation networks.

In the existing DPoD literature several methods are proposed. In [7], Cioffi *et al.* proposed an iterative approach that cancels the nonlinear distortion at the receiver side, referred to as power amplifier nonlinearity cancellation (PANC). Another iterative approach, called reconstruction of distorted signals (RODS) [5], is proposed where rather than cancelling the nonlinear distortion terms, they are included in the signal detection. Both of these methods build on iterative processing tha can be computationally intensive.

DPoD in cellular downlink particularly requires computationally feasible algorithms for parameter estimation and distortion cancellation that can be applied in real-time at the user equipment (UE). This thesis presents a reduced complexity EVM enhancement method that avoids iterative processing assumed in [5], [7]. Furthermore, presented approach does not require any prior knowledge of transmitter nonlinearity characteristics, instead we estimate the nonlinearity characteristics of the transmitter based on the existing downlink demodulation reference signal (DM-RS) which is already used for estimation of multipath channel parameters. The work presented in this thesis and the corresponding FR2 over-the-air experiment results are published at IEEE WAMICON 2023 [8].

The rest of the thesis is organized as follows. In Chapter 2, the theoretical background and some fundamental information required to follow the thesis are briefly presented, including 5G NR physical layer overview, PA basics and performance metrics, PA modeling, and transmitter side linearization techniques. In Chapter 3, two of the receiver side nonlinearity reduction techniques, namely PANC and RODS are discussed along with the presented approach, referred to as Digital Post-Inverse (DPoI). The performance analysis of the reference approach, PANC, and DPoI under various circumstances are conducted through computer simulations using MATLAB software, which are presented in Chapter 4. Finally, the conclusions and the final remarks are discussed in Chapter 5.

2. THEORETICAL BACKGROUND AND FUNDAMENTALS

2.1 5G NR Physical Layer Overview

2.1.1 CP-OFDM

Orthogonal Frequency Division Multiplexing (OFDM) was introduced by Robert W. Chang in 1966 [9] and it has been adopted in 4G LTE downlink transmission scheme, also found to be a suitable waveform for 5G NR. The basic idea is dividing available bandwidth W into N_{act} narrow subchannels, each having width of $\Delta f = W/N_{act}$, also known as subcarrier spacing. Then the data symbols are transmitted in parallel by modulating each subcarrier.

For a parallel block of N_{act} symbols, $a_k, k \in \{0, 1, 2, 3, ..., N_{act} - 1\}$, complex baseband continuous-time waveform of one OFDM symbol duration, T_{sym}, is expressed as

$$x(t) = \frac{1}{\sqrt{N_{act}}} \sum_{k=0}^{N_{act}-1} a_k e^{j2\pi f_k t} = \frac{1}{\sqrt{N_{act}}} \sum_{k=0}^{N_{act}-1} a_k e^{j2\pi k \Delta f t}, 0 \leq t < T_{sym}, \tag{2.1}$$

where $f_k = k\Delta f$ denotes the centre frequency of k-th subcarrier.

Restricting the waveform to the time window of $[0, T_{sym}]$ with rectangular windowing results in a convolution with sinc function in frequency domain. The subcarrier spectra is hence not well band-limited and different subcarriers overlap. By appropriate selection of the subcarrier spacing, the subcarriers can be made orthogonal which enables simple separation of these overlapping subcarriers and allows high spectral efficiency.

Assuming the subcarrier spacing is equal to inverse of the OFDM symbol duration, i.e. $\Delta f = 1/T_{sym}$, any two subcarriers are orthogonal, given by

$$\begin{aligned} \int_{T_{sym}} e^{2\pi k \Delta f t} (e^{2\pi l \Delta f t})^* dt = \int_{T_{sym}} e^{2\pi k \Delta f t} e^{-2\pi l \Delta f t} dt = \int_{T_{sym}} e^{2\pi (k-l) \Delta f t} dt \\ = \begin{cases} T_{sym} & k = l. \\ 0 & \text{otherwise.} \end{cases} \end{aligned} \tag{2.2}$$

This also allows the data symbols to be demodulated at the receiver with a bank of matched filters. However, a more practical and common approach to implement OFDM

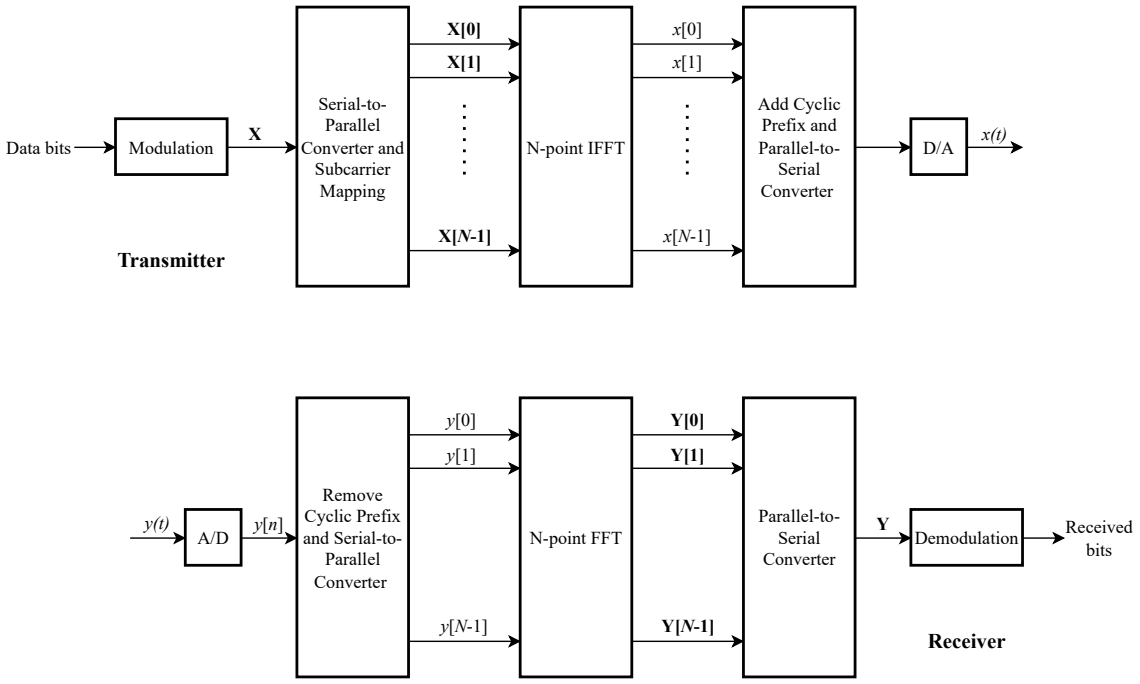

Figure 2.1. *OFDM Transmitter and Receiver Implementation using IFFT/FFT*

transmitter/receiver is using inverse discrete Fourier transform (IDFT)/discrete Fourier transform (DFT) based operation, as illustrated in Figure 2.1.

Sampling the complex baseband continuous-time OFDM transmit signal given in 2.1 at time instants $t = nT_{sym}/N_{act}$ gives

$$x(nT_{sym}/N_{act}) = \frac{1}{\sqrt{N_{act}}} \sum_{k=0}^{N_{act}-1} a_k e^{j2\pi k\Delta f nT_{sym}/N_{act}}. \tag{2.3}$$

Substituting $\Delta f = 1/T_{sym}$ 2.3 results in

$$x(nT_{sym}/N_{act}) = \frac{1}{\sqrt{N_{act}}} \sum_{k=0}^{N_{act}-1} a_k e^{j2\pi kn/N_{act}}. \tag{2.4}$$

Defining the N-point DFT definition of sequence $x(n)$ and corresponding IDFT as

$$\mathbf{X}(\mathbf{k}) = \mathsf{DFT}[x(n)] = \sum_{n=0}^{N-1} x(n) e^{-j2\pi kn/N}, \quad k = 0, 1, ..., N-1 \tag{2.5}$$

$$x(n) = \mathsf{IDFT}[\mathbf{X}(\mathbf{k})] = \frac{1}{\sqrt{N}} \sum_{k=0}^{N-1} \mathbf{X}_{\mathbf{k}} e^{j2\pi kn/N}, \quad n = 0, 1, ..., N-1, \tag{2.6}$$

which implies that OFDM transmitter and receiver can be implemented with IDFT and

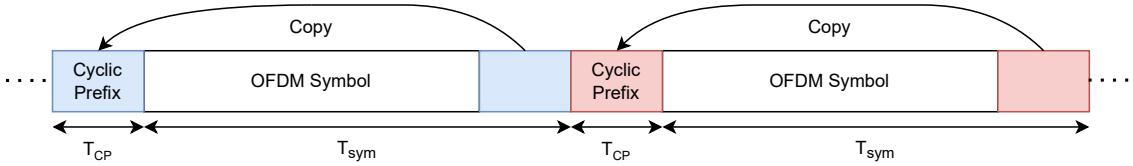

Figure 2.2. *Cyclic Prefix in OFDM*

DFT operations, respectively.

Transmitting an OFDM signal in a multipath channel causes inter symbol interference (ISI). The purpose of cyclic prefix (CP) is to eliminate these problems by acting like a guard space between successive symbols. A cyclic prefix is a copy of the last part of an OFDM symbol that is appended to the beginning of the OFDM symbol as illustrated in Figure 2.2. The length of CP should be longer than the delay spread of the channel to avoid ISI.

Inserting a cyclic prefix also converts the linear convolution with the channel into a cyclic convolution. A cyclic convolution in time domain is equivalent to scalar multiplication in frequency domain, so the frequency domain equalization becomes easier.

Consider a sequence $x(n) = x(0), x(1), ..., x(N-1)$ of length N and discrete time channel with finite impulse response (FIR) $h(n) = h(0), h(1), ..., h(L)$ of length $L+1$. The cyclic prefix for $x(n)$ is the last N_{CP} symbols of $x(n)$, which are attached to the beginning of the sequence. The new sequence becomes $\tilde{x}(n) = x(N-N_{CP}), ..., x(N-1), x(0), ...x(N-1)$ of length $N+N_{CP}$. If $\tilde{x}(n)$ is input to the channel, the channel output $r(n)$, in the absence of noise, is then

$$\begin{aligned} r(n) &= \tilde{x}(n) * h(n) \\ &= \sum_{m=0}^{L} h(m)\tilde{x}(n-m) \\ &= \sum_{m=0}^{L} h(m)x(n-m)_N \\ &= x(n) \circledast h(n) = \text{DFT}[\mathbf{X(k)}]\text{DFT}[\mathbf{H(k)}]. \end{aligned} \tag{2.7}$$

While inserting cyclic prefix is beneficial due to reasons defined above, it does not come without a cost. Adding a copy of the last N_{CP} symbols of an OFDM symbol with a length of N to the beginning of an OFDM symbol naturally causes an overhead of N_{CP}/N, which will result in a reduction in symbol rate. Having a large N is desired to reduce the overhead caused by the cyclic prefix, since the minimum length of cyclic prefix limited by the channel delay spread. However, increasing N also has drawbacks such as increase in transceiver complexity, processing delay and more importantly, PAPR of the transmitted signal, which will be discussed next. For the sake of simplicity, throughout the thesis, a

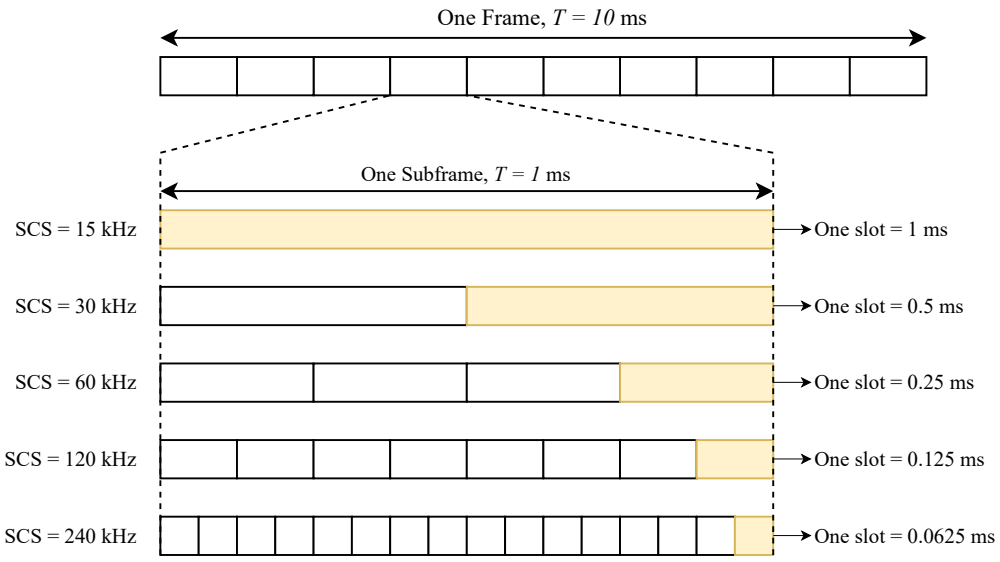

Figure 2.3. *Frames, subframes, and slots.*

discrete time OFDM symbol with CP attached will be denoted as $x(n)$.

2.1.2 Time Domain Structure

NR uses a basic time unit T_c to provide consistent and exact timing definitions. The basic time unit T_c can be thought as the sampling time of an FFT/IFFT-based transmitter/receiver with a subcarrier spacing of 480 kHz and FFT size of 4096 and it is calculated as [10]

$$T_c = \frac{1}{\Delta f \cdot N_{\text{FFT}}} = \frac{1}{480 \times 10^3 \cdot 4096} \approx 0.51\, ns. \tag{2.8}$$

The longest time domain structure of NR is *frame* and it has a duration of $19660800T_c = 10\ ms$. Each frame is identified by a higher level parameter, *System Frame Number (SFN)*. The SFN is a 10-bit number and ranges from 0 to 1023, thus it repeats itself after 1024 frames.

Each frame is divided into equally sized *subframes* which has a duration of $1966080T_c = 1\ ms$. Each subframe is further divided into *slots*. The number of slots a subframe contains ranges from 1 to 16, depending on the numerology. However, the duration of subframe does not depend on numerology and it is always equal to 1 ms.

A slot in NR consists of a fixed number OFDM symbols and it has a dynamic duration. The length of an OFDM symbol is equal to $1/\Delta f$, thus slot duration depends on the chosen numerology. In the case of normal cyclic prefix length, a slot is consisted of 14 OFDM symbols, whereas for the extended cyclic prefix, 12 consecutive OFDM symbols form a slot. Since the subcarrier spacing is scaled by powers of two, a slot essentially can be

Table 2.1. *Supported Numerologies [10]*

μ	$\Delta f = 2^{\mu} \cdot 15$ **kHz**	**Cyclic Prefix**
0	15	Normal
1	30	Normal
2	60	Normal, Extended
3	120	Normal
4	240	Normal

Table 2.2. *Frame structure for different numerologies [10]*

μ	**0**	**1**	**2**	**3**	**4**	**3**
$\Delta f = 15 \times 2^{\mu}$ **kHz**	15	30	60	120	240	60
Cyclic prefix	Normal	Normal	Normal	Normal	Normal	Extended
Slots per subframe	1	2	4	8	16	4
Symbols per slot	14	14	14	14	14	12
Symbol duration (T_c)	131072	65536	32768	16384	8192	32768
Cyclix prefix (T_c)	9216	4608	2304	1152	576	8192
Symbol duration (μs)	66.66	33.33	16.66	8.33	4.16	16.66
Cyclic prefix (μs)	4.69	2.34	1.17	0.58	0.29	4.16

considered to be divided into two equal parts for the next higher numerology, as illustrated in Figure 2.3. Scaling by powers of two has the benefit of maintaining slot boundaries between different numerologies which in turn simplifies mixing different numerologies on the same carrier [11]. The details of the time domain structure used in 5G for different numerologies are listed in Table 2.2.

2.1.3 Frequency Domain Structure

In order to be able to support wide range of applications and usage scenarios, NR supports a flexible OFDM numerology. A numerology is identified by a subcarrier spacing configuration, denoted by μ, along with the cyclic prefix. A list of supported transmission numerologies is given in Table 2.1.

A *resource element* is the smallest physical resource which consists of one subcarrier during one OFDM symbol. Furthermore, a group of twelve consecutive subcarriers forms a *resource block*. It is important to note that the NR definition of resource block is one-dimensional, unlike LTE definition which defines a resource block as twelve subcarriers during one LTE slot duration [11].

A group of resource blocks that covers the full carrier bandwidth in the frequency domain with a duration of one subframe in the time domain is described as *resource grid* [11].

Table 2.3. *Transmission bandwidth configuration for FR1 in terms of number of resource blocks [13]*

Subcarrier Spacing (kHz)	5 MHz	10 MHz	15 MHz	20 MHz	25 MHz	30 MHz	40 MHz	50 MHz	60 MHz	70 MHz	80 MHz	90 MHz	100 MHz
15	25	52	79	106	133	160	216	270	-	-	-	-	-
30	11	24	38	51	65	78	106	133	162	189	217	245	273
60	-	11	18	24	31	38	51	65	79	93	107	121	135

Table 2.4. *Transmission bandwidth configuration for FR2 in terms of number of resource blocks [13]*

Subcarrier Spacing (kHz)	50 MHz	100 MHz	200 MHz	400 MHz
60	66	132	264	-
120	32	66	132	264

There is one resource grid per subcarrier spacing configuration, antenna port, and transmission direction (downlink, uplink, or sidelink); and there is one set of resource grids per tranmission direction [10].

The transmission bandwidth of 5G can be defined as a set of resource blocks on which the base station transmits and receives [12]. Tables 2.3 and 2.4 show the transmission bandwidth configuration in terms of number of resource blocks for each channel bandwidth and subcarrier combination for FR1 and FR2, respectively. To limit the implementation complexity of the user equipment, an NR carrier can be consisted of absolute maximum of 275 resource blocks. [11].

In NR, not all devices need to support the whole channel bandwidth and it is possible that multiple numerologies exist in the same channel bandwidth. Thus, for a device to identify the location of resource block in a channel bandwidth, a common reference point is required, and this point is known as *point A*. Also, for each numerology used in a cell, a numbering scheme is defined through *common resource blocks (CRBs)*, in which the resource blocks are numbered in an increasing order starting from 0 with increasing frequency. The zeroth subcarrier of CRB 0 in each of the numerologies aligned at point A. It is not necessary that point A is located within the actual carrier and its location is signaled to the device as a part of the broadcast system information. To describe the actual transmitted signal, the term *physical resource blocks (PRBs)* is used, and their location is either expressed relative to point A or in terms of CRBs.

As mentioned before, a device in NR does not need to support the whole transmission bandwidth of the base station, rather it can use a smaller part of the whole bandwidth. A set of consecutive physical resource blocks of a specific numerology that is used at device reception is called a *bandwidth part (BWP)*. For example, a device can use narrower bandwidth part to monitor control channels, and the bandwidth part used for data

transmission can be adjusted based on the throughput requirements, resulting in a better power consumption handling for user devices.

2.1.4 Reference Signals

There are several types of reference signals in NR to be used for different purposes by a receiving unit. There are seven types of NR reference signals: demodulation reference signals (DM-RS), phase-tracking reference signals (PT-RS), CSI reference signals (CSI-RS), tracking reference signals (TRS), sounding reference signals (SRS), positioning reference signals (PRS), and remote interference management reference signal (RIM-RS) [10], [11]. Each of the reference signals is briefly described as follows:

- DM-RS is intended for channel estimation. It can be transmitted with physical downlink shared channel (PDSCH), physical uplink shared channel (PUSCH), physical downlink control channel (PDCCH), physical uplink control channel (PUCCH), and physical broadcast channel (PBCH).
- PT-RS can be considered as an extension of DM-RS for PDSCH and PUSCH and used for phase noise and common phase error compensation, thus it plays a crucial role especially in mm-wave frequencies. It has a low density in frequency domain and high density in time domain.
- CSI-RS exists only in downlink direction and it is used by user equipment to acquire the channel-state information (CSI).
- TRS is a reference signal that consists of multiple periodic CSI-RS and it is used by the user equipment to track the time and frequency variations.
- SRS is an uplink-only signal and it is used by base stations to obtain channel-state information (CSI).
- PRS is a downlink reference signal and intended to support positioning.
- An gNB uses RIM-RS to measure inter-cell interference and to provide information about the experienced interference to other gNBs.

Among others, DM-RS for PDSCH is in particular interest of this work due to its configuration flexibility and being transmitted in each slot, thus it is discussed in details in the next section.

Demodulation Reference Signal (DM-RS) for PDSCH

For a range of deployment scenarios and use cases, the DM-RS in NR offers a lot of flexibility: it has a front-loaded design for low latency, supports up to 12 orthogonal antenna ports for MIMO, transmission durations can range from 2 to 14 symbols, and supports up to four reference signals per slot [11]. The parameters used to configure DM-RS can be

categorized under the parameters that control sequence generation and the parameters that control the mapping to physical resources.

For CP-OFDM scheme, a pseudo-random sequence, namely Gold sequence of length $2^{31}-1$, is used to generate DM-RS sequence. Irrespective of the BWP used for data transmission, the sequence is generated for whole CRBs in the frequency domain, but transmitted only in the BWP used for data transmission. By generating the reference signal sequence for whole CRBs, it is ensured that multiple devices scheduled on overlapping time-frequency resources in the case of MU-MIMO will follow the same underlying sequence. The parameters that control the sequence generation are DM-RS scrambling identity ($N_{ID}^{n_{SCID}}$), DM-RS scrambling initialization (n_{SCID}), OFDM symbol number within the slot (l), and slot number within a frame ($n_{s,f}^{\mu}$). The details of sequence generation is described in TS 38.211 Section 5.2.1, and Section 7.4.1.1.1 [10].

The parameters that control the mapping to physical resources can be further divided into two groups whether they control the time domain resources or frequency domain resources. The main parameter that controls time domain resources is *the mapping type*. The mapping type can be either *type A (slot-wise)* or *type B (non-slot-wise)*. Further, the parameters *DM-RS type A position*, *DM-RS length*, and *DM-RS additional position* are used to define the allocation of DM-RS to time domain resources and their values depend mainly on mapping type.

DM-RS type A position indicates the location of the first DM-RS OFDM symbol (l_0) within a slot. For mapping type A, l_0 can be either 2 or 3, whereas for mapping type B, l_0 is always 0. The definition of DM-RS OFDM symbol locations are also different for mapping type A and mapping type B. For mapping type A, the DM-RS OFDM symbol locations are defined relative to the first OFDM symbol of the slot. For mapping type B, on the other hand, the definitions are done relative to the first OFDM symbol of allocated PDSCH resources. DM-RS length controls the length of DM-RS symbol as a single symbol DM-RS or double symbol DM-RS. The number of additional DM-RS OFDM symbols allocated is configured by DM-RS additional position parameter and can take values between 0 and 3, depending on the mapping type, DM-RS length, and PDSCH symbol allocation. The locations of additional DM-RS OFDM symbols are given in TS 38.211 Tables 7.4.1.1.2-3 and 7.4.1.1.2-4 [10].

The parameters that control the frequency domain resources are *DM-RS configuration type* and *DM-RS antenna ports*. Subcarrier locations of DM-RS symbols are defined as [10]

$$k = \begin{cases} 4m + 2k' + \Delta & \text{Configuration type 1} \\ 6m + k' + \Delta & \text{Configuration type 2} \end{cases} \tag{2.9}$$

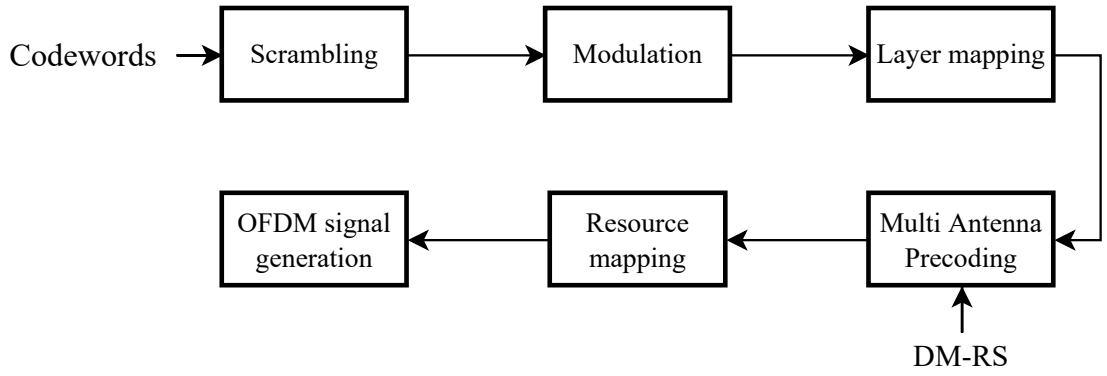

Figure 2.4. *Physical channel processing for PDSCH*

where k is the subcarrier index and $m = 0, 1, \ldots$, $k' = 0, 1$. Δ represents the delta shift applied to the subcarriers used, and its value depends on the DM-RS configuration type and DM-RS antenna ports. The values that Δ can take are given in TS 38.211 Tables 7.4.1.1.2-1 and 7.4.1.1.2-2 [10].

2.1.5 Overview of Downlink Physical-Channel Processing

The downlink physical channel processing steps are illustrated in Figure 2.4 [10], [12].

The codewords are first scrambled and modulated. The supported modulation schemes include QPSK, 16QAM, 64QAM and 256QAM in downlink [10]. Then, the layer mapping step distributes the modulation symbols to different transmission layers such that every nth symbol is mapped to the nth layer. Transmission layers are then mapped to a set of antenna ports with a precoding matrix. It is important to note that DM-RS goes through same precoding as data symbols, which means the receiver does not need to know which precoding matrix is used at the transmitter, it is rather seen as part of the channel. Then, the precoded symbols are mapped to the set of available resource blocks assigned by the MAC scheduler and finally OFDM signal generation takes place to generate transmit waveform.

2.2 Peak-to-Average Power Ratio of an OFDM Signal

One of the major drawbacks of the OFDM systems is high Peak-to-Average Power Ratio (PAPR) of the transmitted signals. Having a high PAPR is not desired since it negatively affects transmitter power amplifier efficiency. Furthermore, since the amplitude of a high PAPR signal has larger dynamic range, it is required to employ an ADC with high resolution at the receiver which results in an increased complexity and power consumption for the receiver front-end [14].

The PAPR of a continuous time signal is defined as

$$\text{PAPR}[x(t)] \triangleq \frac{\max|x(t)|^2}{\mathbf{E}[|x(t)|^2]}, \quad 0 \leq t \leq T_{sym}. \tag{2.10}$$

Similarly, for a discrete-time signal, PAPR is defined as

$$\text{PAPR}[x(n)] \triangleq \frac{\max|x(n)|^2}{\mathbf{E}[|x(n)|^2]}, \quad 0 \leq n \leq N-1. \tag{2.11}$$

Consider a set of data symbols a_k, $k = 0, 1, ...N_{act} - 1$, and then an OFDM signal during an arbitrary symbol interval, $x(n)$, is generated as (neglecting the scaling for simplicity)

$$x(n) = \sum_{k=0}^{N_{act}-1} a_k e^{j2\pi kn/N_{act}}, \quad 0 \leq n \leq N-1. \tag{2.12}$$

Assuming that data symbols are independent and they all have same energy, E_s, average power of $x(n)$ is given by

$$\mathbf{E}[|x(n)|^2] = \sum_{k=0}^{N-1} \mathbf{E}[|a_k|^2] = NE_s. \tag{2.13}$$

The maximum value of $|x(n)|^2$ occurs when all the data symbols a_k add coherently, resulting in

$$\max(|x(n)|^2) = (N\sqrt{E_s})^2 = N^2E_s. \tag{2.14}$$

As a result, the maximum PAPR of an OFDM transmission signal is determined as

$$\text{PAPR}[x(n)] = \frac{N^2E_s}{NE_s} = N. \tag{2.15}$$

As mentioned before, it is desired to have large N in an OFDM system and hence, coherent addition of N data symbols is highly improbable in practice. This implies that the PAPR of a practical OFDM system will be significantly lower than N. At this point, it is more meaningful to investigate the statistical distribution of PAPR of an OFDM system. It is stated in [15] that if N is sufficiently large ($N \geq 64$), OFDM signals converge to a complex Gaussian process by the Central Limit Theorem. The envelope of the OFDM signal then has a Rayleigh distribution with zero mean and variance $\sigma^2/2 = P_{av}/2$ where P_{av} is the average power of the OFDM signal [15]. Therefore, the probability that the PAPR exceeds a threshold $P_0 = \sigma_0^2/\sigma^2$ is given as [14],

$$p(\text{PAPR}[x(n)] \geq P_0) = 1 - (1 - e^{-P_0})^N, \quad 0 \leq n \leq N. \tag{2.16}$$

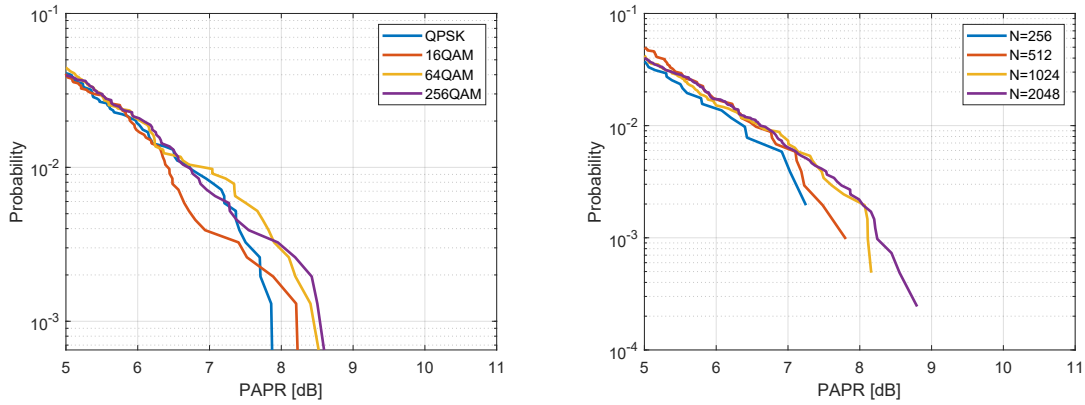

(a) *PAPR CCDF with varying modulation order, $N = 512$*

(b) *PAPR CCDF with varying N, 64QAM modulation*

Figure 2.5. *PAPR CCDF of an OFDM signal with different modulation orders and N*

which implies that PAPR increases with increasing N, even if the theoretical maximum value is not reached in practice.

2.3 Power Amplifier Basics and Performance Metrics

Power amplifier (PA) is one of the key elements in a wireless system. Its role is to amplify the input RF signal while keeping the distortion under a certain level such that reliable detection at the receiver is possible. PAs are often the limiting element of the overall performance of a wireless system [16], therefore it is important to describe PA performance through some performance metrics. PA performance can be evaluated in terms of PA power gain, power efficiency, linearity, noise floor and TX leakage, bandwidth, robustness against antenna mismatches, and module size and cost [17], all of which contribute to the overall performance of the wireless system, but power gain, power efficiency, and linearity are particularly in the scope of this work to describe PA performance. Consequently, these performance metrics are presented along with their relation to the overall system performance in the first section, then followed by power amplifier modeling approaches.

2.3.1 Power Gain

Power gain of a PA is simply defined by the ratio of output power to the input power and it is usually represented in logarithmic units [18]:

$$G_{dB} = 10 \log_{10} \left(\frac{P_{\text{out}}}{P_{\text{in}}} \right). \tag{2.17}$$

Transmitted power mainly depends on the PA, hence PA must provide sufficient gain to satisfy link-level requirements. Ideally, a power amplifier should provide a constant gain

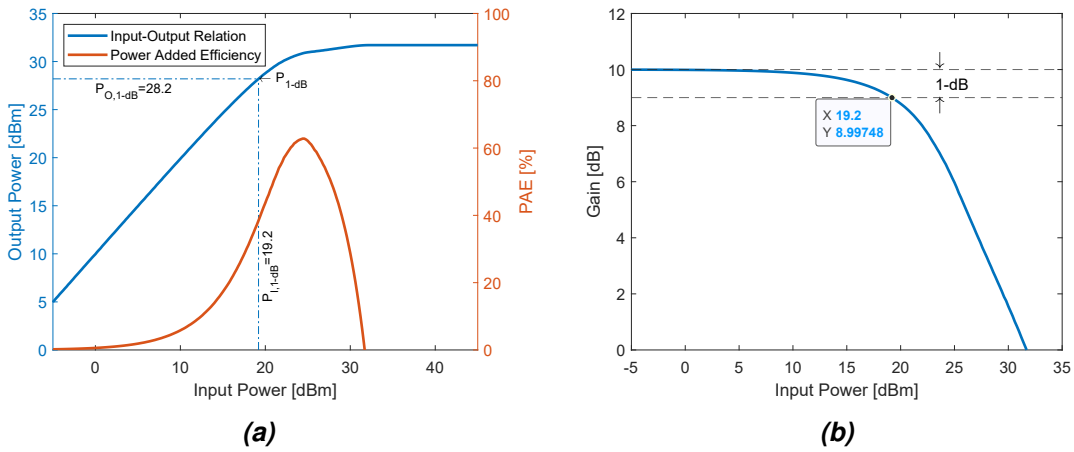

Figure 2.6. *(a) An example PA input-output power curve and PAE, (b) and corresponding amplifier power gain.*

for all input power levels. However, power amplifiers are inherently nonlinear devices, and this leads to a non-constant gain since it depends on input/output power at which it is evaluated [19]. Figure 2.6 illustrates the input-output relation of a PA and the nonlinear behaviour of gain. The region where the gain is almost constant is called *linear* region. As the input power increases, the PA is driven into compression and no longer be able to provide a constant gain. An important figure of merit, 1-dB compression point ($P_{\text{1-dB}}$), is defined as the point where the actual gain is decreased by 1 dB with respect to linear gain [19]. Corresponding input power and output power levels can be referred to as $P_{\text{I,1-dB}}$ and $P_{\text{O,1-dB}}$, respectively, and shown in Figure 2.6.

2.3.2 Efficiency

From an energy point-of-view, a PA can be considered as a component that converts DC supply power (P_{DC}) into RF output power (P_{out}), driven by an input power (P_{in}) [18]. Power efficiency, η, is a metric that describes the effectiveness of this conversion, defined as

$$\eta = \frac{P_{\text{out}}}{P_{\text{DC}}}. \tag{2.18}$$

The definition in 2.18is often referred to as *drain efficiency (DE)*. For low gain power amplifiers, DE definition may be misleading since it does not take power gain, or input power, into account. An alternative definition which takes also the input power into account, *power added efficiency (PAE)*, is defined as [20]

$$\eta_{\text{PAE}} = \frac{P_{\text{out}} - P_{\text{in}}}{P_{\text{DC}}} = \frac{P_{\text{out}}}{P_{\text{DC}}}\left(1 - \frac{1}{G}\right), \tag{2.19}$$

where G represents PA gain in linear scale. It can be easily noticed that both expres-

sions converge for high-gain power amplifiers, whereas PAE tends to be more accurate to describe practical efficiency for low-gain power amplifiers.

A power amplifier with high power efficiency is highly desired in any wireless transmitter, since it often dominates the overall system efficiency. For a fixed RF output power, power efficiency in a way determines the DC supply power consumption, which is of utmost importance especially for battery-based devices such as mobile phones. Also, for a fixed DC supply power, PA with high efficiency allows higher output power. It also allows the use of smaller cooling equipment as the non-converted portion of the DC supply power is mainly dissipated as heat.

As can be seen from Figure 2.6a, the maximum efficiency is achieved when the PA is operating close to its saturation region, where the nonlinear behaviour of PA significantly effective. This immediately results in a trade-off between efficiency and linearity, since both features are crucial to overall system performance.

2.3.3 Linearity

Ideally, a PA is expected to amplify the power of the input signal without introducing any distortion. However, due to PAs being naturally nonlinear devices, distortion-free amplification is inevitable. Also, operating close to saturation region due to efficiency concerns causes PA to have further nonlinear behaviour. This nonlinear behaviour is particularly critical for nonconstant envelope signals such as high-order QAM modulated signals.

The distortion caused by nonlinear PA can be classified into in-band distortion and out-of-band distortion [17]. In-band distortion affects amplitude and phase of the signal in the desired frequency range, leading to a degradation of bit-error-rate and error-vector-magnitude, eventually reducing Quality-of-Service of the wireless. Out-of-band distortion causes an unwanted spectral regrowth of the transmitted signal which leads to a leakage to adjacent channels in cellular networks.

PA nonlinearity can be described in terms of AM/AM and AM/PM conversion and these are often obtained via measurements [21]. The former represents the distortion in the amplitude of the output signal whereas the latter represents the distortion in the phase of the output signal, as a function of the input signal amplitude. An example is illustrated in Figure 2.7.

2.4 Power Amplifier Modeling

It is necessary to have an accurate model of a power amplifier in order to overcome its detrimental effects. PA modeling approaches can be divided into three groups: physics based, circuit based, and black box (behavioral) modelling[22].

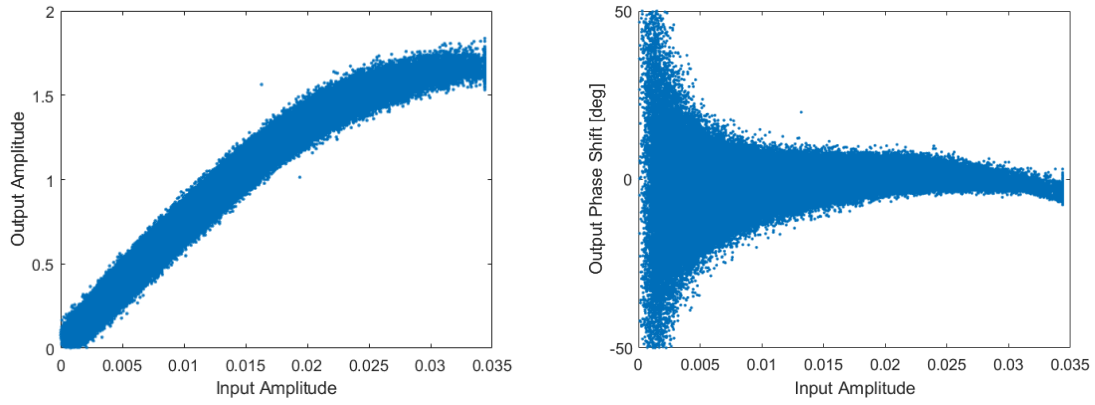

Figure 2.7. *(a) AM/AM and (b) AM/PM distortion of a power amplifier with memory effects*

Physics based approach uses the fundamental physical laws to model the PA and, circuit based approach uses an equivalent circuit representation of the PA. However, these two approaches are computationally too intensive and require a detailed information of the internal structure of the PA, which may not be always available.

When such an information is not available, blackbox models, or behavioral models, are desired. These models are computationally efficient and may assume no *a priori* information of the internal structure of the PA [23]. This approach builds the model of the PA by relating its input and output signals in the form of relatively simple mathematical expressions. Hence, the accuracy of these models are sensitive to data set and mathematical expression used during the model extraction procedure. It is possible that the extracted model for one class of data set to be inaccurate for another class of data set with different statistical properties.

A very straightforward way to describe the nonlinear behaviour of a PA is relating its input signal, $x(t)$, to its output signal, $y(t)$, with a nonlinear function $f(.)$. There are various forms (or models) that explicitly defines the nonlinear function $f(.)$. These models can be classified into two major groups[24]: memoryless models, where the nonlinear function $f(.)$ is described as static, and memory models, where the nonlinear function $f(.)$ is described as dynamic.

2.4.1 Memoryless Nonlinear Models

Memoryless models are used to characterize a PA whose output depends only on the instantaneous value of the input signal. In this case, PA output $y(t)$ can be simply expressed as a function of its input signal $x(t)$ as

$$y(t) = f(x(t)), \tag{2.20}$$

where $f(.)$ represents a nonlinear function. A narrowband passband input signal centered around ω_c can be written as

$$x_{RF}(t) = A(t)cos[\omega_c t + \phi(t)] = \mathsf{Re}[x(t)e^{j\omega_c t}], \tag{2.21}$$

where $A(t)$ and $\phi(t)$ represents the envelope and phase components of the input signal, respectively, and complex baseband equivalent input signal representation $x(t)$ is

$$x(t) = A(t)e^{j\phi(t)}. \tag{2.22}$$

Following the mathematical representation in 2.20, the PA output can be written as

$$y_{RF}(t) = f_A(A(t))cos[\omega_c t + \phi(t) + f_P(A(t))], \tag{2.23}$$

where the functions $f_A(.)$ and $f_P(.)$ represent the nonlinear AM/AM and AM/PM conversions, respectively. There are various models exist in the literature to represent nonlinear behaviour of a memoryless PA. In the next parts, two commonly used examples of those models, namely complex power series model and Saleh model are presented.

Power Series Model

A general P-th order power series memoryless model of a nonlinear PA can be expressed as [24]

$$y(t) = \sum_{p=1}^{P} c_p x(t)^p, \tag{2.24}$$

where $x(t)$ and $y(t)$ represent the RF input and output signals of the PA and c_p denotes the coefficient of p-th order nonlinearity. Power series model is a useful tool to analyze the harmonic and intermodulation products of a nonlinear PA with two-tone input signal and it is shown in the following. A two-tone input signal can be expressed as

$$x_{RF}(t) = Acos[\omega_c t + \phi] = A_1 cos[\omega_1 t + \phi_1] + A_2 cos[\omega_2 t + \phi_2], \tag{2.25}$$

where A_1, A_2, ϕ_1), ϕ_2, ω_1, ω_2 denote the amplitudes, phases and the angular frequencies of the two input tones. Assuming a third-order power series for simplicity, PA model can be expressed as

$$y_{RF}(t) = c_1 x_{RF}(t) + c_2 x_{RF}^2(t) + c_3 x_{RF}^3(t). \tag{2.26}$$

Substituting 2.25 into 2.26 yields

$$\begin{aligned} y_{RF}(t) = & c_1\{A_1 cos[\omega_1 t + \phi_1] + A_2 cos[\omega_2 t + \phi_2]\} \\ & + c_2\{A_1 cos[\omega_1 t + \phi_1] + A_2 cos[\omega_2 t + \phi_2]\}^2 \\ & + c_3\{A_1 cos[\omega_1 t + \phi_1] + A_2 cos[\omega_2 t + \phi_2]\}^3. \end{aligned} \tag{2.27}$$

The two tone output in decomposed form, using basic trigonometric identities, can be written as

$$\begin{aligned} y_{RF}(t) = & c_2 A_1 A_2 + c_2 A_1 A_2\{cos[(\omega_1 - \omega_2)t + (\phi_1 - \phi_2)]\} \\ & + \left(c_1 A_1 + \tfrac{9}{4} k_3 A_1^3\right) cos(\omega_1 t + \phi_1 t) + \left(c_1 A_2 + \tfrac{9}{4} k_3 A_2^3\right) cos(\omega_2 t + \phi_2) \\ & + \tfrac{3}{4} c_3 A_1^2 A_2[cos((2\omega_1 - \omega_2)t + (2\phi_1 - \phi_2))] \\ & + \tfrac{3}{4} c_3 A_2^2 A_1[cos((2\omega_2 - \omega_1)t + (2\phi_2 - \phi_1))] \\ & + c_2 A_1 A_2 cos((\omega_1 + \omega_2)t + (\phi_1 + \phi_2)) \\ & + \tfrac{1}{2} c_2 A_1^2 cos(2\omega_1 t + 2\phi_1) + \tfrac{1}{2} c_2 A_2^2 cos(2\omega_2 t + 2\phi_2) \\ & + \tfrac{1}{4} c_3 A_1^3 cos(3\omega_1 t + 3\phi_1) + \tfrac{1}{4} c_3 A_2^3 cos(3\omega_2 t + 3\phi_2). \end{aligned} \tag{2.28}$$

It can be seen from 2.28 that the PA output signal consists of spectral components at DC, the fundamental frequencies ω_1 and ω_2, harmonics at $2\omega_1$, $2\omega_2$, $3\omega_1$, and $3\omega_2$, the second-order intermodulation products at $\omega_1 \pm \omega_2$ and lastly, the third-order intermodulation products at $2\omega_1 \pm \omega_2$ and $2\omega_2 \pm \omega_1$. An illustration of these components is depicted in Figure 2.8, assuming that two input tones have equal power, i.e. $A_1 = A_2 = A$.

Next, if we assume a more general bandpass input signal instead of a two-tone input signal, which can be expressed as

$$x_{RF}(t) = A(t) cos(\omega_c t + \phi(t)). \tag{2.29}$$

The corresponding PA output signal is

$$\begin{aligned} y_{RF}(t) = & \frac{1}{2} c_2 A^2(t) + \left(c_1 A(t) + \frac{3}{4} c_3 A^3(t)\right) cos(\omega_c t + \phi(t)) \\ & + \frac{1}{2} c_2 A^2(t) cos(2\omega_c t + 2\phi(t)) \\ & + \frac{1}{4} c_3 A^3(t) cos(3\omega_c t + 3\phi(t)). \end{aligned} \tag{2.30}$$

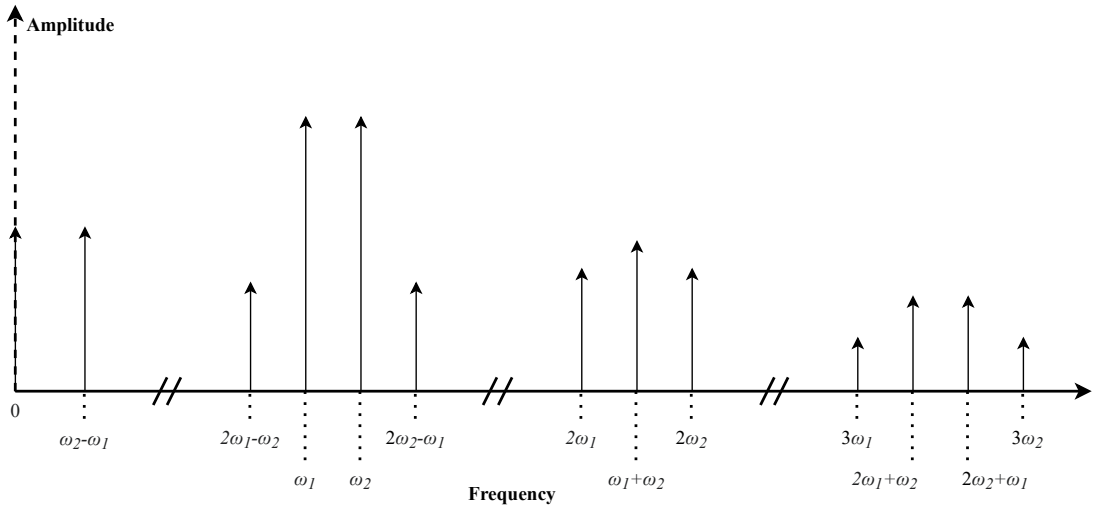

Figure 2.8. *Frequency components of the output of a PA modeled by a memoryless third-order power series with two equipowered input tones.*

It can be easily seen that only the odd-order nonlinear products fall on to the fundamental frequency, hence even-order nonlinearities are irrelevant and will not be considered in the following. If the envelope of the input signal $A(t)$ is non-constant, as in the case for modulated signals, then 2.30 shows that there is a spectral regrowth at the nonlinear PA output since $\frac{3}{4}c_3A^3(t)$ has generally higher bandwidth than $c_1A(t)$. For PA modeling and digital predistortion processing, if we consider a complex baseband equivalent of the input signal, that is $x = A(t)e^{j\phi(t)}$, the complex baseband representation of the PA output is

$$\begin{aligned} y(t) &= \bar{c}_1 A(t)e^{j\phi(t)} + \bar{c}_3 A^3(t)e^{j3\phi(t)}. \\ &= \bar{c}_1 x(t) + \bar{c}_3 \left|x(t)\right|^2 x(t), \end{aligned} \tag{2.31}$$

where $\bar{c}_i$ represents the complex coefficient of i-th nonlinearity of baseband model. It is easy to generalize 2.31 to higher order odd nonlinearities in a similar form, i.e. $\left|x(t)\right|^4 x(t)$, $\left|x(t)\right|^6 x(t), \ldots$, which are extensively used in both PA modeling and digital predistortion processing. An illustration of spectral regrowth due to nonlinear PA is illustrated in Fig. 2.9 for both passband and baseband.

Complex power series model has been an attractive approach, especially considering its ease of implementation. Since the polynomial approximation is linear in parameters, that is, the coefficients c_p are not part of the nonlinear expression, it is possible to use straightforward least-squares to determine these coefficients [2]. However, although the modeling errors tend to decrease with increasing polynomial degree, after some point it is observed that the errors begin to increase again. It is also important to note that complex power series model can be disastrous outside the amplitude domain of measured data.

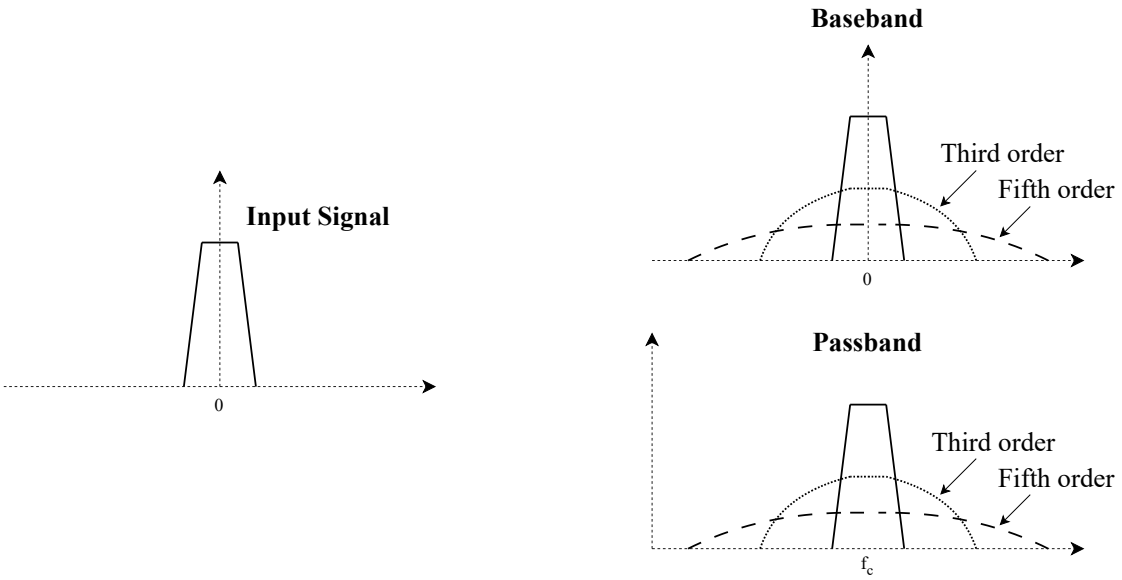

Figure 2.9. *An example of output spectrum of a nonlinear PA that shows the spectral regrowth. Only odd order nonlinearities are considered.*

Saleh Model

The model was proposed by Saleh in [25] as simple two-parameter formulas for modeling the AM/AM and AM/PM characteristics and initially targeted modeling travelling-wave tube (TWT) amplifiers. Representing the input signal $x_{RF}(t)$ as

$$x_{RF}(t) = A(t)cos[\omega_c t + \phi(t)], \tag{2.32}$$

and the output signal $y_{RF}(t)$ as

$$y_{RF}(t) = f_a[A(t)]cos\{\omega_c t + \phi(t) + f_p[A(t)]\}. \tag{2.33}$$

Then, the AM/AM and AM/PM modeling functions are given as

$$f_a(r) = \frac{\alpha_a r}{1 + \beta_a r^2} \tag{2.34}$$

$$f_p(r) = \frac{\alpha_p r^2}{1 + \beta_p r^2}, \tag{2.35}$$

respectively, where α_a, β_a, α_p, and β_p are the fitting parameters.

Saleh model later has been applied to solid-state power amplifiers; however, it was less successful to provide adequate accuracy. To overcome the problems related to application to solid-state power amplifiers, modified Saleh models have been proposed, but they

are not covered in this thesis.

2.4.2 Nonlinear Models with Memory

In the case where the input signal bandwidth is comparable with the power amplifier's inherent bandwidth, the PA exhibits a frequency-dependent response. This kind of phenomenon is referred to as *memory effects* and the conventional memoryless methods fail to accurately model such PAs. The output signal not only depends on the instantaneous value of the input signal, but also depends on the past time instances of the input signal. The input-output relation of the PA can now be expressed with a forced nonlinear differential equation [24]:

$$f\left(y(t), \frac{dy(t)}{dt}, \ldots, \frac{d^k y(t)}{dt^k}, x(t), \frac{dx(t)}{dt}, \ldots, \frac{dy^l(t)}{dt^l}\right) = 0. \tag{2.36}$$

Since the models are generally evaluated in a digital computer, it is convenient to adopt a discrete-time representation. Assuming that the signals are sampled with a sampling period T_s, i.e. $t \to nT_s$, 2.36 can be expressed in a recursive form as

$$y(n) = f_R\left(y(n-1), \ldots, y(n-M_1), x(n), x(n-1), \ldots, x(n-M_2)\right). \tag{2.37}$$

It is also possible to represent the relation in a non-recursive form, with a desirable small error [24], as

$$y(n) = f_D\left(x(n), x(n-1), \ldots, x(n-M)\right). \tag{2.38}$$

Although there are various approaches to model the functions $f_R(.)$ and $f_D(.)$, two of these approaches gained particular popularity, namely polynomial or Volterra series based forms and artificial neural networks (ANN). In the following, Volterra series based models are presented; the latter is out-of-scope of this thesis and majority of the existing approaches use the non-recursive form, hence not included in the following section.

Wiener Model

The Wiener model is a two-box model that contains a linear dynamic block followed by a static nonlinear block, as illustrated in Figure 2.10a.

Assuming that the linear dynamic block is represented by an discrete-time FIR filter, the input-output relation can be written as

$$u_W(n) = \sum_{d=0}^{D-1} h(d)x(n-d), \tag{2.39}$$

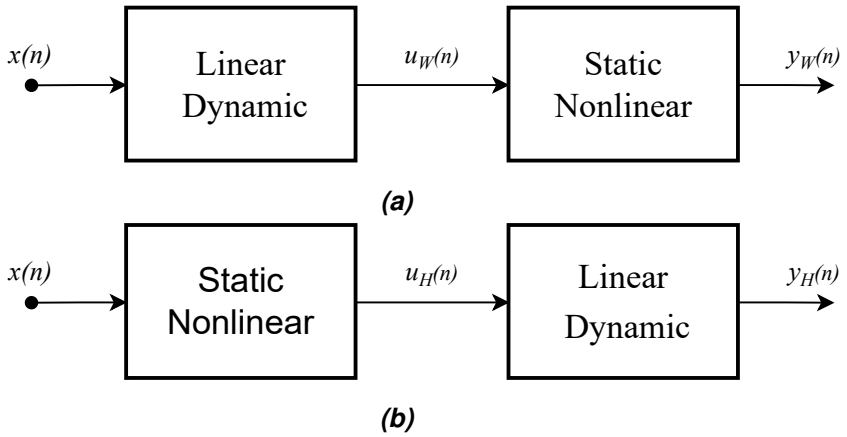

Figure 2.10. *(a)The Wiener model. (b) The Hammerstein model.*

and the polynomial representation of the static nonlinear block is

$$y_W(n) = \sum_{p=0}^{P} c_p u_W(n)|u_W(n)|^p. \tag{2.40}$$

The overall baseband model can be described by combining 2.39 and 2.40 as

$$y_W(n) = \sum_{p=0}^{P} c_p \left[\sum_{d=0}^{D} h(d)x(n-d) \left| \sum_{d=0}^{D} h(d)x(n-d) \right|^p \right]. \tag{2.41}$$

Hammerstein Model

Similar to Wiener model, Hammerstein model is also a two-box model where the blocks are placed in reverse order, static nonlinear block is followed by a linear dynamic block, as illustrated in Figure 2.10b.

The input-output relation of static nonlinear block again can be expressed with a polynomial representation as

$$u_H(n) = \sum_{p=0}^{P} c_p x(n)|x(n)|^P, \tag{2.42}$$

and the input-output relation of linear dynamic block is

$$y_H(n) = \sum_{d=0}^{D} h(d)u_H(n-d). \tag{2.43}$$

The overall baseband model output is obtained by combining 2.42 and 2.43 as

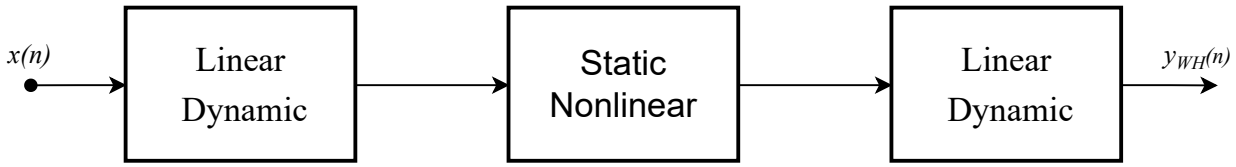

Figure 2.11. *The Wiener-Hammerstein model.*

$$y_H(n) = \sum_{d=0}^{D} h(d) \left[\sum_{p=0}^{P} c_p x(n-d)|x(n-d)|^p \right]. \tag{2.44}$$

Wiener-Hammerstein Model

The Wiener-Hammerstein model is a three-box model constructed by placing a linear dynamic block before and after the static nonlinear block as depicted in Figure 2.11.

Assuming that static nonlinear block is described with a polynomial and two linear dynamic blocks are represented by two FIR filters, the overall response of the Wiener-Hammerstein model can be expressed as

$$y_{WH} = \sum_{d_2=0}^{D_2-1} h_2(d_2) \sum_{p=0}^{P} c_p \left[\sum_{d_1=0}^{D_1-1} h_1(d_1) x(n-d_2-d_1) \left| \sum_{d_1=0}^{D_1-1} h_1(d_1) x(n-d_2-d_1) \right|^p \right], \tag{2.45}$$

where $h_1(d_1)$ and $h_2(d_2)$ denotes the impulse response functions of the first and second FIR filters, respectively.

Volterra Series Based Models

Volterra series was first introduced by Vito Volterra in 1887 as a representation of any nonlinear system with memory. A well known representation of any causal linear system with memory in terms of its impulse response $h(\tau)$ is

$$y(t) = \int_{-\infty}^{+\infty} h(\tau) x(t-\tau) d\tau, \tag{2.46}$$

where $x(t)$ and $y(t)$ denotes the input and the output signals of the system. Also recalling the power series representation of a memoryless nonlinear system as

$$y(t) = \sum_{i=1}^{\infty} c_i x(t)^i, \tag{2.47}$$

where $x(t)$, $y(t)$, and c_i are the input, output, and i-th order nonlinearity, respectively.

The continuous-time domain Volterra series representation of a nonlinear system with memory is obtained by combining the expressions 2.46 and 2.47, and expressed as [26]

$$\begin{aligned} y(t) =& h_0 + \int_{-\infty}^{+\infty} h_1(\tau_1)x(t-\tau_1)d\tau_1 \\ &+ \int_{-\infty}^{+\infty}\int_{-\infty}^{+\infty} h_2(\tau_1,\tau_2)x(t-\tau_2)d\tau_1 d\tau_2 + \dots \\ &+ \int_{-\infty}^{+\infty}\dots\int_{-\infty}^{+\infty} h_p(\tau_1,\dots,\tau_p)x(t-\tau_1)\dots x(t-\tau_p)d\tau_1\dots d\tau_p + \dots \end{aligned} \tag{2.48}$$

where $h_p(\tau_1,\dots,\tau_p)$ is often called *Volterra kernels*. For example, for $p=1$, $h_p(\tau)$ is the linear impulse response of the system described in 2.46. Similarly, the Volterra kernels with $p>1$ are used to characterise the nonlinearity of corresponding order.

For PA modeling and linearization purposes, it is convenient the use discrete-time complex baseband representation with finite memory depth and finite nonlinearity order and it can be written as [27]

$$\begin{aligned} y(n) =& \sum_{i=0}^{M} h_1(i)(n-i) \\ &+ \sum_{i_1=0}^{M}\sum_{i_2=i_1}^{M}\sum_{i_3=0}^{M} h_3(i_1,i_2,i_3)x(n-i_1)x(n-i_2)x^*(n-i_3) \\ &+ \sum_{i_1=0}^{M}\sum_{i_2=i_1}^{M}\sum_{i_3=i_2}^{M}\sum_{i_4=0}^{M}\sum_{i_5=i_4}^{M} h(i_1,i_2,i_3,i_4,i_5)\times \\ & x(n-i_1)x(n-i_2)x(n-i_3)x^*(n-i_4)x^*(n-i_5) + \dots \end{aligned} \tag{2.49}$$

where $x(n)$ and $y(n)$ are the baseband input and output signals, respectively, and $h_p(i_1,i_2,\dots,i_p)$ is the complex Volterra kernel. Redundant items associated with kernel symmetry and, the even-order kernels are omitted in 2.49.

Volterra series is a powerful model that can represent the nonlinear behaviour of a PA with high accuracy. However, it is often stated that effectiveness of Volterra series is limited to weakly nonlinear systems [24] due to convergense issues under strong nonlinearity. Also, the computational complexity of Volterra series increases exponentially with increasing nonlinearity order and memory depth, which makes it not suitable for real-time applications. Volterra based simplified models such as memory polynomial (MP), and generalized memory polynomial (GMP) provide good modeling capacity while having a reduced computational complexity, and they are presented in the following.

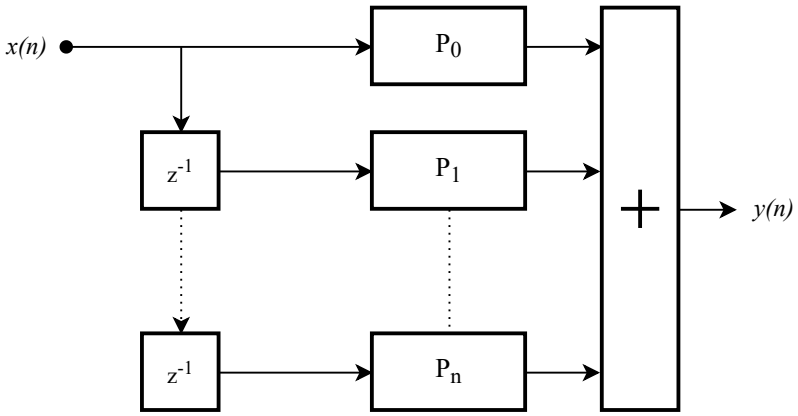

Figure 2.12. *The memory polynomial model.*

Memory Polynomial Model

The memory polynomial (MP) is a simplified version of Volterra series to represent a nonlinear PA with memory effects. It consists of a delay line and a set of polynomial functions, and the output is equal to the sum of the outputs of the polynomial functions. The structure of memory polynomial modes is depicted in Figure 2.12, and the discrete-time baseband MP model can be mathematically expressed as [28]

$$y(n) = \sum_{p=1}^{P} \sum_{d=0}^{D} c_{p,d} x(n-d)|x(n-d)|^{p-1}, \tag{2.50}$$

where P and D are the nonlinearity order and memory depth, respectively, and $c_{p,d}$ represents the complex coefficent of p-th order and d-th delayed nonlinearity. The memory polynomial model can be described as a Volterra series model including only the *diagonal* terms [2].

Generalized Memory Polynomial Model

The Generalized Memory Polynomial (GMP) model was proposed by Morgan in [29] and it is an extended version of the memory polynomial model that also includes the cross-terms between the signal and its lagging and/or leading exponentiated envelope. A discrete-time baseband representation of the GMP model is

$$
\begin{aligned}
y(n) = & \sum_{k=0}^{K_a-1} \sum_{l=0}^{L_a-1} a_{kl} x(n-l)|x(n-l)|^k \\
& + \sum_{k=1}^{K_b} \sum_{l=0}^{L_b-1} \sum_{m=1}^{M_b} b_{klm} x(n-l)|x(n-l-m)|^k \\
& + \sum_{k=1}^{K_c} \sum_{l=0}^{L_c-1} \sum_{m=1}^{M_c} c_{klm} x(n-l)|x(n-l+m)|^k,
\end{aligned}
\tag{2.51}
$$

where, $K_a L_a$, $K_b L_b M_b$, and $K_c L_c M_c$ are the number of coefficients for aligned signal and envelope, signal and lagging envelope, and signal and leading envelope, respectively.

2.5 Transmitter Side Linearization Techniques

In order to increase power efficiency, a PA can be forced into its nonlinear operating region, which typically produces unwanted spectral regrowth into adjacent channels, which can eventually lead to violations of the out-of-band (OOB) emissions regulations. Consequently, a PA linearization technique at the transmitter side is essential to satisfy the spectral masking requirements.

There are three general techniques for transmitter side PA linearization: the feedback, the feedforward and the predistortion techniques [16]. The feedback linearization technique is one of the simplest method that uses a feedback loop to mitigate the nonlinear distortion caused by PA. The nonlinear distortion is obtained by feeding back the PA output signal to compare it with the input signal and then it is destructively combined with the PA output to obtain a linearly amplified signal. The drawback of the feedback linearization is that it is not applicable for wideband signals. Feedforward linearization technique, on the other hand, can handle signals with broader bandwidths. The PA input signal is feedforwarded to be compared with an attenuated version of the PA output signal to obtain the distortion signal. The distortion signal is then amplified back with a linear amplifier to be subtracted from the PA output signal to obtain a linearly amplified signal. Due to usage of two amplifiers, feedforward methods have a poor efficiency, and they are relatively complex to design [16].

Predistortion is one of the most used methods in commercial PA applications due to its low complexity and high efficiency [16]. The principle of operation is that a predistorter (PD) is placed before a nonlinear PA such that a linearly amplified signal is obtained at the output of this combined structure. Theoretically, if the PD is modeled by the inverse of the nonlinear PA model, their combination ensures a linear amplification. Implementation can be done in analog domain, digital domain, or as a hybrid type. Analog predistortion (APD) can be applied directly in front of the PA structure, and can be more cost effective for appli-

cations requiring large bandwidths [30]. However, due to its flexibility and accuracy, digital predistortion (DPD) is the most used technique in commercial applications and it is implemented at digital front-end [2]. It provides an accurate inverse characteristics of the PA, and it can be implemented in an adaptive manner such that DPD parameters are updated continuously to be adjusted to the changes of PA characteristics over time. However, DPD has some drawbacks. First of all, since DPD is a part of digital front-end processing, in the feedback loop that contains the PD parameters extraction processing, the analog PA output signal is needed to be down-converted to baseband and transformed into digital domain. Due to the fact that PD being an inherently nonlinear device that causes spectral regrowth, upsampling is necessary to accommodate this increased bandwidth. Although the upsampling rate to be used depends on the input signal bandwidth and application-specific predistortion capability, if a PA with fifth-order dominant nonlinearity is considered as an example, it is required to use upsampling rate of 5 in a conventional DPD implementation in order to capture the nonlinear effects [1]. This, however, also means that the components in the DPD feedback processing chain such as ADCs and digital-to-analog converters (DACs) in the forward path should be able to support a much wider bandwidth than the input signal bandwidth. Furthermore, these ADCs should have a large resolution to ensure a good linearization performance. ADCs with high sampling rate and large resolution ultimately increases the overall power consumption and component cost. Moreover, mmWave frequencies are started to be utilized in 5G NR where up to 400 MHz of signal bandwidth can be supported, and very short wavelength of mmWave frequencies results in a reduction in physical antenna size which eventually allows large antenna array systems to be employed. From DPD implementation perspective, however, this means further increase in complexity, cost and power consumption. As an alternative approach, linearization can be performed at the receiver side. In the next chapter, several receiver side linearization techniques existing in the literature are briefly presented in addition to proposed receiver side linearization technique.

3. RECEIVER SIDE NONLINEARITY REDUCTION TECHNIQUES

3.1 PANC

In [7], Cioffi *et al.* proposed an iterative approach to cancel the nonlinear distortion at the receiver side, called power amplifier nonlinearity cancellation (PANC). They consider a memoryless PA and it is assumed that the PA model parameters are perfectly known at the receiver.

The idea of PANC is to estimate *distortion term* $d(n)$ in the received signal by using the initial estimate of PA input $x(n)$. After that, distortion term is subtracted from the received signal to obtain a better estimation of $x(n)$, and this process is performed iteratively. An illustration of PANC technique is given in Figure 3.1, and assuming that the received symbols $\mathbf{Y_k}$, frequency domain channel estimate $\mathbf{H_k}$, and frequency domain distortion term $\mathbf{D_k^m}$; m-th estimation of the transmitted symbols ($\mathbf{X_k^m}$), initializing with $\mathbf{D^0} = 0$, is given in Table 3.1.

There exist several works that extend the PANC algorithm. In [31], PANC algorithm is combined with channel and nonlinear distortion estimation. Similarly, in [32], FD-TD-PANC is proposed, where PANC is combined with frequency- and time-domain channel estimation. Finally, PANC with PA model parameter estimation and channel estimation is presented in [33].

Table 3.1. *PANC algorithm.*

1. $\mathbf{X_k^{(m)}} = \left\langle \frac{\mathbf{Y_k}}{\mathbf{H_k}} - \mathbf{D^{(m-1)}} \right\rangle$
2. $x(n)^{(m)} = \mathsf{IFFT}(\mathbf{X}^{(m)})$
3. $d(n)^{(m)} = f(x(n)^{(m)}) - x(n)^{(m)}$
4. $\mathbf{D}^m = \mathsf{FFT}(d(n)^{(m)})$

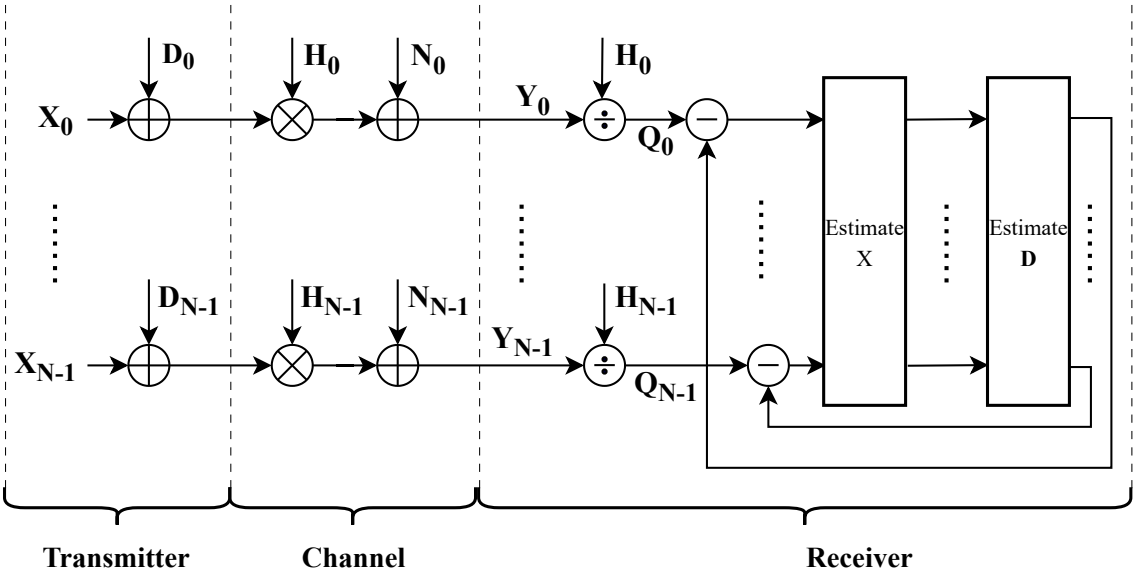

Figure 3.1. *Block diagram of PANC method.*

Table 3.2. *RODS algorithm.*

1.	Calculate the time domain signal :	$x(n)^{(m)} = \text{IDFT}(\mathbf{X}^{(m)})$
2.	Calculate the signal's instantaneous power :	$\gamma^{(m)^T} = \left(\lvert x_0^{(m)}\rvert, \lvert x_{N-1}^{(m)}\rvert\right)$
3.	Estimate $\underline{\underline{K}}^{(m)}$ as given in [5] Appx. A	
4.	Least Squares solution for $\mathbf{X}^{(m)}$:	$\mathbf{X}^{(m)} = \left(\underline{\underline{K}}^{*^{(m)}}\underline{\underline{K}}^{(m)}\right)^{-1}\underline{\underline{K}}^{*^{(m)}}\tilde{\mathbf{X}}$

3.2 RODS

In [5], an iterative approach, referred to as *Reconstruction Of Distorted Signals* (RODS), is proposed. Instead of estimating and removing the nonlinear distortion from the received signal, RODS aims to detect the nonlinear received signal by reconstructing it. Similar to PANC approach, in [5] it is also assumed that the nonlinear parameters are known at the receiver.

Given that the received symbols are denoted as $\tilde{\mathbf{X}}$, and the initial estimation of transmitted symbols is expressed as $\mathbf{X}^{(0)} = \tilde{\mathbf{X}}/\mu_{\text{RODS}}$, where μ_{RODS} is given in [5] Appendix B, the summary of RODS algorithm is given in Table 3.2. It is stated that RODS provides a better performance than both PANC and ideal DPD. On the other side, computational complexity of RODS is extremely high compared to other methods, thus we consider it to be not feasible for real-time applications and do not include any simulation or numerical results related to RODS.

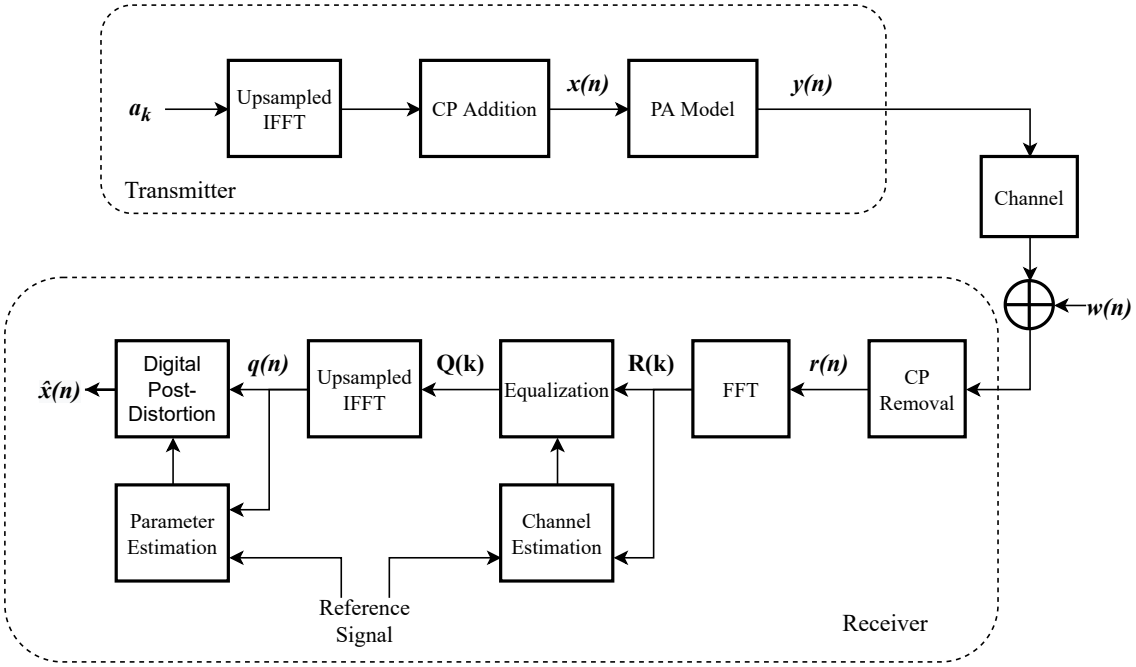

Figure 3.2. *Block diagram of Digital Post-Inverse method.*

3.3 Digital Post-Inverse

In this section, we describe a non-iterative, one-shot method to mitigate the nonlinear passband effects of the transmitter, referred to as Digital Post-Inverse (DPoI). DPoI does not require any *a priori* knowledge of the transmitter nonlinear model parameters. Also, being a one-shot method allows DPoI to be computationally less complex compared to other approaches such as PANC and RODS. A block diagram describing DPoI is given in Figure 3.2, and the procedure is presented below.

3.3.1 System Model

On the transmitter side, considering FFT/IFFT based CP-OFDM transmission scheme, the discrete-time representation of the OFDM signal in any OFDM symbol duration can be written as

$$x(n) = \frac{1}{\sqrt{N}} \sum_{k=-N_{act}/2}^{N_{act}/2} a_k e^{j2\pi kn/N}, \quad -N_{CP} \leq n \leq N, \tag{3.1}$$

where a_k represents the M-QAM modulated data symbols on the active subcarriers $k \in \{-N_{\text{act}}/2, \ldots, N_{\text{act}}/2\}$. It is assumed that the subcarrier spacing is Δf, and sampling rate is $f_s = \Delta f \varepsilon N_{\text{FFT}}$, where ε represents the oversampling factor and N_{FFT} is the fundamental FFT size. Each useful OFDM symbol then consists of $N = \varepsilon N_{\text{FFT}}$ time domain samples, and $x(n)$ is obtained by appending cyclic prefix of length N_{CP}.

In order to model transmitter nonlinear distortion, we utilize a memory polynomial. The distorted signal $y(n)$ hence can be represented as

$$y(n) = \sum_{\substack{p=1 \\ p \text{ odd}}}^{P_{\text{TX}}} \sum_{d=0}^{D_{\text{TX}}} c_{p,d} x(n-d)|x(n-d)|^{(p-1)}, \tag{3.2}$$

where P_{TX} and D_{TX} represent the nonlinearity order and memory depth of transmitter, respectively, and $c_{p,d}$ is the complex coefficient for p-th order and d-th delayed nonlinearity.

After that, the transmit waveform passes through a multipath channel with additive white Gaussian noise (AWGN). The signal at the receiver front-end, $r(n)$, can be written as

$$r(n) = h(n) * y(n) + w(n), \tag{3.3}$$

where $h(n)$ and $w(n)$ are the channel impulse response and AWGN, respectively. Here, we assume that the receiver operates at a sampling rate of $f_{s,\text{RX}} = N_{\text{FFT}}$, and the received signal is transformed into frequency domain via N_{FFT}-point FFT operation after CP removal, resulting in a frequency domain representation as

$$\mathbf{R}(\mathbf{k}) = \mathbf{H}(\mathbf{k})\mathbf{Y}(\mathbf{k}) + \mathbf{W}(\mathbf{k}), \tag{3.4}$$

where $\mathbf{R}(\mathbf{k})$, $\mathbf{H}(\mathbf{k})$, $\mathbf{Y}(\mathbf{k})$, and $\mathbf{W}(\mathbf{k})$ are the FFTs of received signal, channel impulse response, transmit waveform, and AWGN term, respectively. Next, frequency domain linear equalization is utilized to mitigate the channel effects. Frequency domain representation of the equalizer output is

$$\begin{aligned} \mathbf{Q}(\mathbf{k}) &= \mathbf{H}_{\text{est}}\mathbf{R}(\mathbf{k}) \\ &= \mathbf{H}_{\text{est}}\mathbf{H}(\mathbf{k})\mathbf{Y}(\mathbf{k}) + \mathbf{H}_{\text{est}}\mathbf{W}(\mathbf{k}), \end{aligned} \tag{3.5}$$

where $\mathbf{H}_{\text{est}}$ and $\mathbf{Q}(\mathbf{k})$ represent the estimated channel frequency response and the FFT of the signal at the equalizer output, respectively. Then, the signal is transformed back to time-domain via N-point IFFT, where $N = \varepsilon N_{\text{FFT}}$. Its time-domain expression can be written as

$$q(n) = \tilde{y}(n) + \tilde{w}(n), \tag{3.6}$$

where $\tilde{y}(n) = \text{IFFT}\left[\mathbf{H}_{\text{est}}\mathbf{H}(\mathbf{k})\mathbf{Y}(\mathbf{k})\right]$ and $\tilde{w}(n) = \text{IFFT}\left[\mathbf{H}_{\text{est}}\mathbf{W}(\mathbf{k})\right]$.

Then, $q(n)$ is *post-distorted* such that an estimate of the desired signal $x(n)$ is obtained by utilizing a memory polynomial model whose input is given as $q(n)$. Time domain representation of the estimate of the desired signal, $\hat{x}(n)$, can be written as

$$\hat{x}(n) = \sum_{\substack{p=1 \\ p \text{ odd}}}^{P_{\mathsf{RX}}} \sum_{d=0}^{D_{\mathsf{RX}}} \tilde{c}_{p,d} q(n-d)|q(n-d)|^{(p-1)}, \tag{3.7}$$

where P_{RX}, D_{RX} are the nonlinearity order and the memory depth of the post-distortion model and the complex coefficient $\tilde{c}_{p,d}$ are called as *inverse* nonlinear coefficients. Lastly, $\hat{x}(n)$ is decimated by a factor of ε and estimates of transmit symbols, $\hat{a}_k$, are obtained for symbol detection by processing $\hat{x}(n)$ through N_{FFT}-point FFT operation.

In the following, the estimation procedure of inverse complex coefficients $\tilde{c}_{p,d}$ is addressed.

3.3.2 Parameter Estimation

In this part, the estimation of complex coefficients which build the *inverse* nonlinear model depicted in 3.7 is presented. Considering a known reference signal exists at the receiver side, it can be used together with the equalized signal $q(n)$ to estimate the *inverse* coefficient $\tilde{c}_{p,d}$ such that inverse nonlinear model would yield the reference signal when these coefficients are applied to the equalized signal. It should be noted that the estimated coefficients are assumed to be constant over a certain interval e.g. one slot (14 OFDM symbols) and they are updated by re-estimating them during each interval.

Denoting the reference signal as x_{ref}, and the corresponding received and equalized signal as q_{ref}, 3.7 can be rewritten as

$$x_{\mathsf{ref}}(n) = \sum_{\substack{p=1 \\ p \text{ odd}}}^{P_{\mathsf{RX}}} \sum_{d=0}^{D_{\mathsf{RX}}} \tilde{c}_{p,d} q_{\mathsf{ref}}(n-d)|q_{\mathsf{ref}}(n-d)|^{(p-1)}. \tag{3.8}$$

At this point, we switch to vector matrix representation for notational convenience. Let $\tilde{\boldsymbol{c}}$ represents the $N_c \times 1$ vector of complex nonlinear coefficients

$$\tilde{\boldsymbol{c}} = \begin{bmatrix} \tilde{c}_{0,0} & \dots & \tilde{c}_{0,D_{\mathsf{RX}}+1} & \dots & \tilde{c}_{p,d} & \dots \tilde{c}_{(P_{\mathsf{RX}}+1)/2,D_{\mathsf{RX}}+1} \end{bmatrix}^T, \tag{3.9}$$

where $N_c = (P_{\mathsf{RX}}+1)(D_{\mathsf{RX}}+1)/2$ is the total number of coefficients. Then, defining the $N \times 1$ basis function vector of p-th order and d-th delayed nonlinearity, $\Upsilon_{p,d}$, as

$$\Upsilon_{p,d}(n) = q_{\text{ref}}(n-d)|q_{\text{ref}}(n-d)|^{p-1}, \tag{3.10}$$

the basis function matrix, $\boldsymbol{\Upsilon}$, of size $N \times N_c$ is constructed such that each column of $\boldsymbol{\Upsilon}$ is represented by a basis function $\Upsilon_{p,d}$ associated with a complex coefficient $\tilde{c}_{p,d}$;

$$\boldsymbol{\Upsilon} = \begin{bmatrix} \Upsilon_{0,0}(n) & \dots & \Upsilon_{0,D_{\text{RX}}+1}(n) & \dots & \Upsilon_{p,d}(n) & \dots \Upsilon_{(P_{\text{RX}}+1)/2,D_{\text{RX}}+1}(n) \end{bmatrix} \tag{3.11}$$

Thus, 3.8 can be written in vector matrix form as

$$\boldsymbol{x}_{\text{ref}} = \boldsymbol{\Upsilon}\tilde{\boldsymbol{c}}, \tag{3.12}$$

where $\boldsymbol{x}_{\text{ref}}$ is the $N \times 1$ vector of time domain samples of known reference signal. It is seen that $\tilde{\boldsymbol{c}}$ is the only unknown in 3.12 and hence can be estimated with least-squares (LS) solution as

$$\tilde{\boldsymbol{c}} = (\boldsymbol{\Upsilon}^H\boldsymbol{\Upsilon})^{-1}\boldsymbol{\Upsilon}^H\boldsymbol{x}_{\text{ref}}. \tag{3.13}$$

It is important to note that a noisy input in inverse model estimation results in a bias in the coefficients [34]. However, our simulation and measurement results show that a significant portion of the nonlinear distortion can be mitigated with this approach, which will be presented in the next chapter.

4. SIMULATION ENVIRONMENT AND NUMERICAL RESULTS

4.1 Simulation Environment

PANC method [7] is chosen to be reference method for performance comparison and both methods are implemented and simulated using MATLAB software. A SISO downlink transmission is considered and, 5G NR standard-compliant waveform generator and receiver processing are constructed with MATLAB 5G Toolbox. DM-RS is found to be a suitable reference signal for parameter estimation described in Section 3.3.2.

On the transmitter side, NR OFDM waveform is generated by following the procedure as explained in Section 2.1.5. In order to properly estimate nonlinear model parameters, it is assumed that the DM-RS carrying OFDM symbol includes only the DM-RS modulation symbols. In other words, there is no frequency-multiplexing with PDSCH modulation symbols, instead the subcarriers which are supposed to carry PDSCH modulation symbols are forced to be zero. The OFDM waveform is then upsampled and fed into a nonlinear PA whose behaviour is modeled by a memory polynomial. In order to reduce to PAPR of the OFDM waveform to a certain range, the signal is first passed through a soft envelope limiter (SEL), whose characteristics is expressed as

$$f_{SEL}(x) = \begin{cases} x & |x| \leq A \\ Ae^{j\phi} & |x| > A, \end{cases} \tag{4.1}$$

where A denotes the maximum allowed instantaneous amplitude of the signal. In the simulations, A is chosen such that the PAPR distribution of the OFDM waveform after soft envelope limiter is limited to 8 dB. After SEL, the signal at PA input is backed-off such that

$$x(t)_{\text{IBO}} = \frac{x(t)}{10^{BO/20}}, \tag{4.2}$$

where BO represents the back-off in decibels. Input back-off (IBO) is defined as

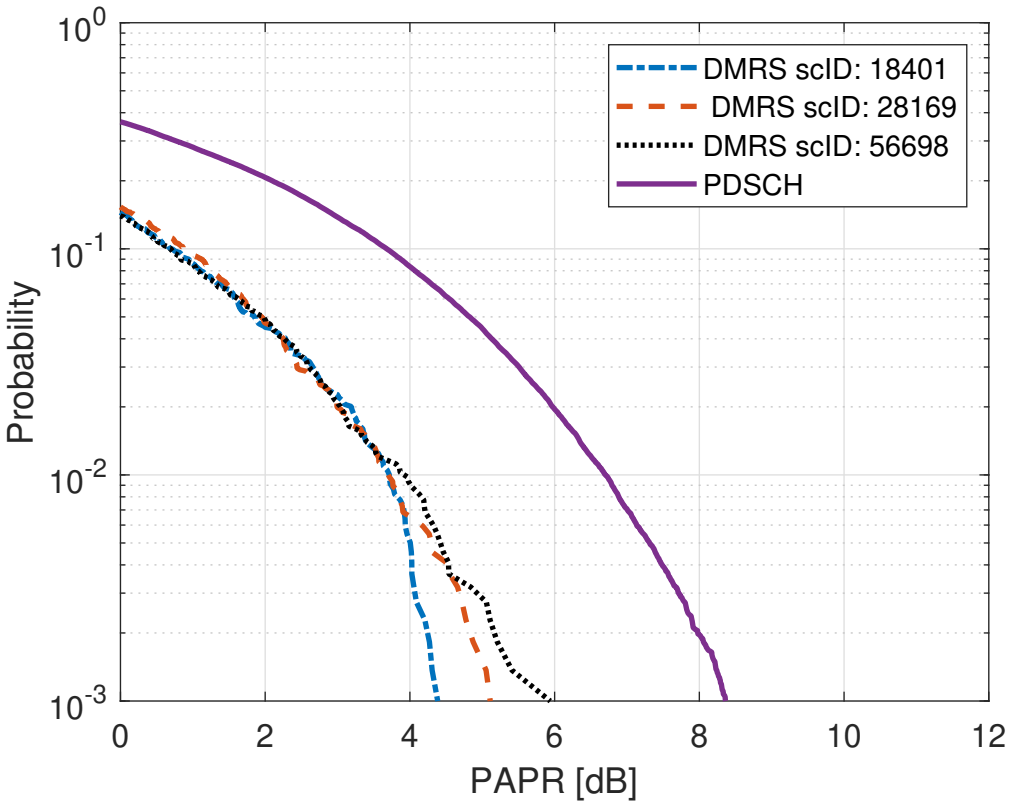

Figure 4.1. *PAPR CCDFs of PDSCH and DM-RS OFDM symbols with different scrambling identities.*

$$\text{IBO} = \frac{P_{\text{in,sat}}}{P_{\text{in,avg}}}, \tag{4.3}$$

where $P_{\text{in,sat}}$ and $P_{\text{in,avg}}$ are the input saturation power of the PA and the average power of the signal at the PA input, respectively.

The PA output is downsampled to original sampling rate before being propagated through channel.

Forcing the subcarriers that are supposed to carry PDSCH modulation symbols in DM-RS carrying OFDM symbol to be zero results in a difference in PAPR distribution between the DM-RS carrying OFDM symbol and the rest of the waveform as depicted in Figure 4.1. Nonlinear model parameters estimated with such a reference signal thus lose their validity when they are used in PANC or DPoI. As a result, we propose a DM-RS boosting approach such that the envelope characteristics of DM-RS carrying OFDM symbol and the rest of the OFDM waveform are matched.

The propagation channel is modeled with a tapped delay line (TDL) channel model, more specifically TDL-E channel model, with parameters given in Table 4.1. Actual delay values can be obtained simply multiplying normalized delay values in Table 4.1 with the desired

Table 4.1. *TDL-E Channel Model [35]*

Tap#	Normalized Delay	Power [dB]	Fading Distribution
1	0	-0.03	LOS path
	0	-22.03	Rayleigh
2	0.5133	-15.8	Rayleigh
3	0.5440	-18.1	Rayleigh
4	0.5630	-19.8	Rayleigh
5	0.5440	-22.9	Rayleigh
6	0.7112	-22.4	Rayleigh
7	1.9092	-18.6	Rayleigh
8	1.9293	-20.8	Rayleigh
9	1.9589	-22.6	Rayleigh
10	2.6426	-22.3	Rayleigh
11	3.7136	-25.6	Rayleigh
12	5.4524	-20.2	Rayleigh
13	12.0034	-29.8	Rayleigh
14	20.6519	-29.2	Rayleigh

RMS delay spread.

On the receiver side, the received signal is OFDM demodulated after CP removal. Then, DM-RS based channel estimation is performed followed by an LMMSE equalizer. The equalized frequency domain symbols are transformed back into time domain via IFFT operation. Then, nonlinear model parameter estimation is done by using equalized DM-RS OFDM symbol as explained in Section 3.3.2. Finally, the equalized signal is post-distorted using the estimated parameters and transformed back into frequency domain for symbol detection.

In their original work, Cioffi *et al.* assumed that nonlinear model parameters of the transmitter is perfectly known at the receiver side [7]. However, in order to make a fair comparison, we assumed that the receiver has no information related to transmitter nonlinearity, instead PA model parameters are estimated at the receiver side employing the same approach described in Section 3.3.2 with proper input-output assignment.

4.2 Numerical Results

In this section, simulation results that shows the performance of PANC and DPoI methods are presented. Error vector magnitude (EVM) is used to evalute the performance of both methods. EVM is calculated as

Table 4.2. *Simulation Parameters*

Waveform	
Bandwidth	200
Subcarrier Spacing	60
Modulation	64QAM / 256QAM
DM-RS Parameters	
Mapping Type	A
Configuration Type	1
DM-RS Length	1
Additional Position	0
Type A Position	2

$$\text{EVM (\%)} = \sqrt{\frac{\frac{1}{N}\sum_{n=1}^{N}(a_{\text{RX}} - a_{\text{TX}})^2}{\frac{1}{N}\sum_{n=1}^{N}(a_{\text{TX}})^2}}. \tag{4.4}$$

where a_{RX} and a_{TX} denotes the received and transmitted QAM symbols, respectively. The parameters used in the simulations are given in Table 4.2. They are divided into groups according to their relation to specific parts of the simulator.

Two sets of simulation results are presented, one is evaluated considering a memoryless PA and the other is evaluated considering a PA with memory. Each result is generated by averaging 100 realizations. Receiver EVM values are calculated with respect to varying input back-off value. A higher input back-off allows the PA to impose less nonlinear distortion, but at the expense of efficiency. It is assumed that the linear channel imposes an AWGN with 20 dB SNR on the transmitted signal. Channel estimation and coefficient estimation are performed with noisy signal, but post-distortion methods are applied to the noiseless signal and their output is taken into account during EVM calculations. Furthermore, an ideally linearized PA model is derived from actual PA input-output relations to be used in the simulations to evaluate the receiver EVM performance under linear conditions. In all simulation cases, it is observed that PANC converges after second iteration, illustrated in Figure 4.2, thus only the second iteration of PANC algorithm is presented in the figures.

4.2.1 Memoryless Power Amplifier

The memoryless power amplifier is modeled with a memory polynomial model simply setting memory depth to zero. Considered PA model has a nonlinearity order of 11 and

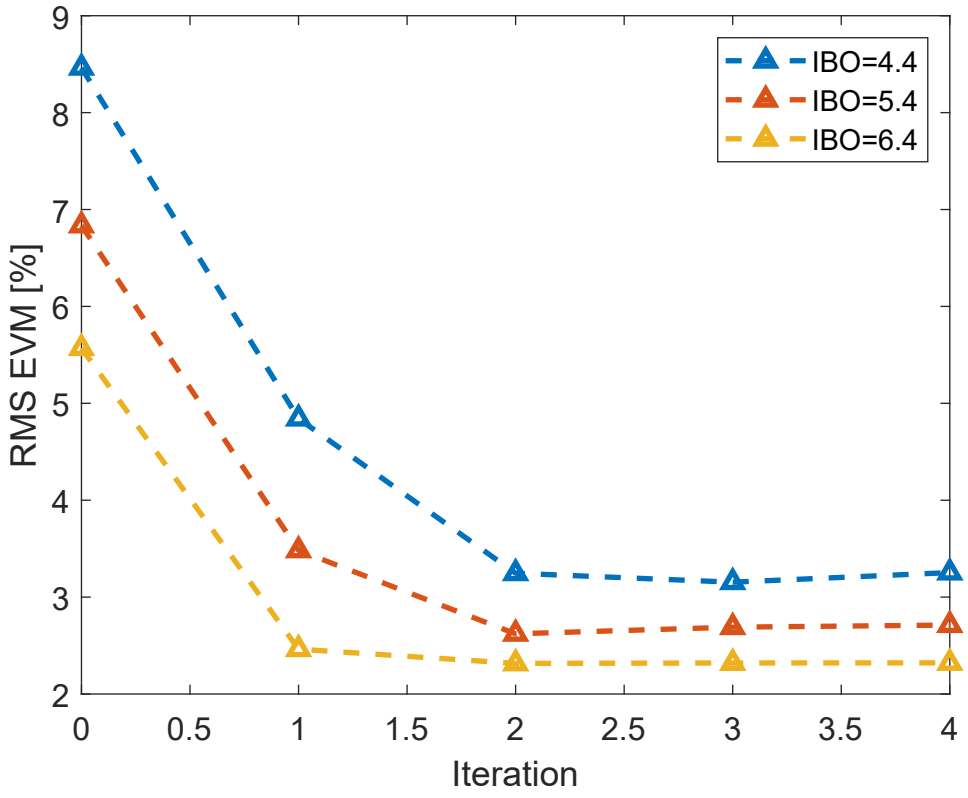

Figure 4.2. *Receiver EVM obtained after each iteration of PANC. 256QAM modulation scheme, memoryless PA, AWGN-only channel.*

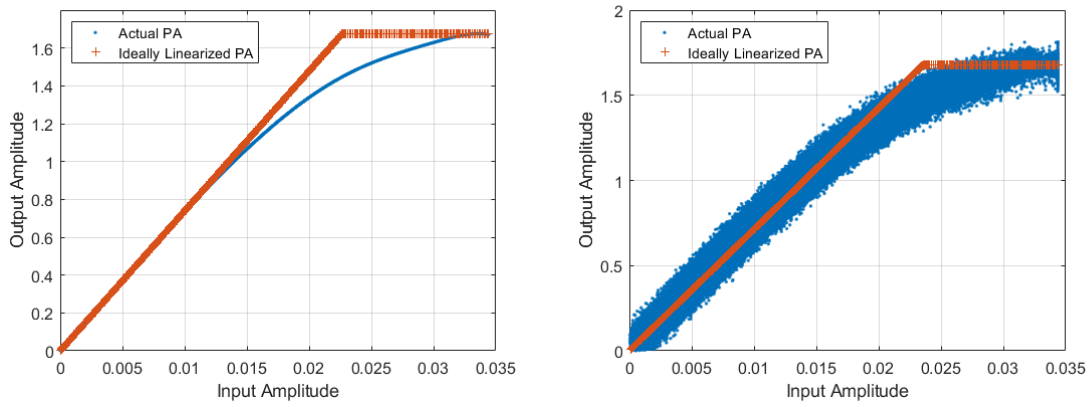

(a) ***(b)***

Figure 4.3. *AM/AM responses of the transmitter PA, and corresponding ideally linearized PA (a) without memory and (b) with memory effects.*

only the odd order nonlinearities are taken into account. The value of each nonlinear complex coefficient of considered PA is given in Table 4.3. AM/AM responses of the considered PA and the corresponding ideally linearized PA are given in Figure 4.3a.

The simulations are first carried out for AWGN-only channel, and the results are presented in Figures 4.4a and 4.4b for 64QAM and 256QAM schemes, respectively. It is seen that

Table 4.3. *Memoryless PA Model Coefficients*

Coefficient	Value
c_1	$1.1413 - j0.0805$
c_3	$-0.0791 + j0.0967$
c_5	$0.0216 - j0.0049$
c_7	$-0.0185 - j0.0163$
c_9	$0.0048 + j0.0046$
c_{11}	$(-3.9489 + j3.6971) \times 10^{-4}$

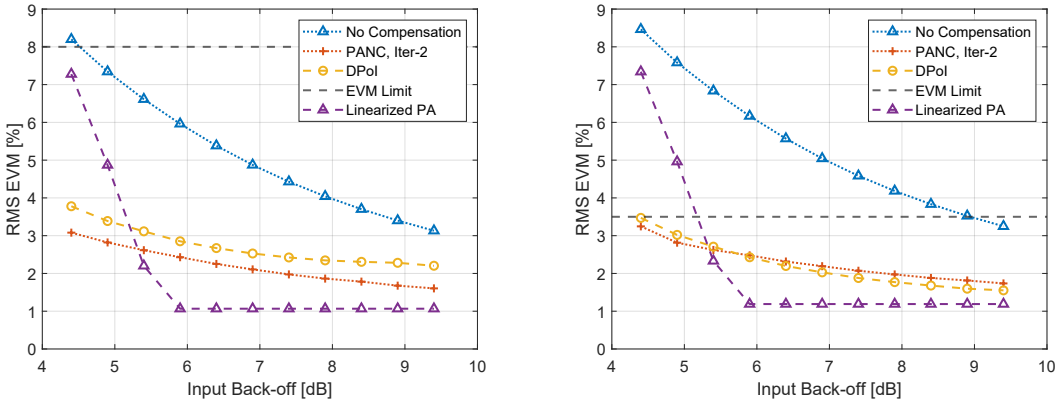

(a) *64QAM* ***(b)*** *256QAM*

Figure 4.4. *EVM simulation results for AWGN-only channel, memoryless PA. Parameter estimation is performed with noisy signal whereas EVM values are calculated from noiseless signal.*

both methods provide a significant enhancement in terms of receiver EVM performance and their performance are similar to each other; PANC overperforms DPoI for 64QAM scheme, whereas DPoI is slightly better than PANC for 256QAM scheme. Between 4 to 6 dB IBO range, PANC and DPoI overperform ideally linearized PA. This is due to the fact that PA input signal has a PAPR distribution that goes up to 8 dB, which in turn results in PA output signal to be saturated at some samples, causing severe nonlinear distortion. For IBO values of 6 dB or larger, the amount of saturated ideally linearized PA output samples are negligibly small, thus receiver EVM values converge around 1% after 6 dB IBO.

Although both post-distortion methods provide a significant improvement, EVM requirement of 8% for 64QAM scheme [36] is satisfied even without any post-distortion methods applied. This situation, however, turns out to be the exact opposite for 256QAM scheme; 3.5% EVM requirement is not achieved without any post-distortion methods applied for almost all IBO values in given range, whereas applying either PANC or DPoI ensures that the receiver EVM is below the specified limit for a given IBO range.

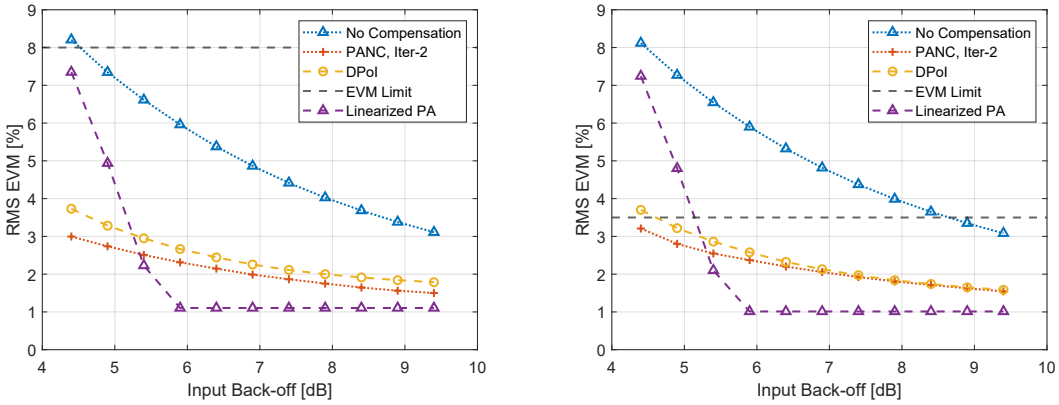

(a) *64QAM* ***(b)*** *256QAM*

Figure 4.5. *EVM simulation results for TDL-E channel with 30 ns RMS delay spread, memoryless PA. Parameter estimation is performed with noisy signal whereas EVM values are calculated from noiseless signal.*

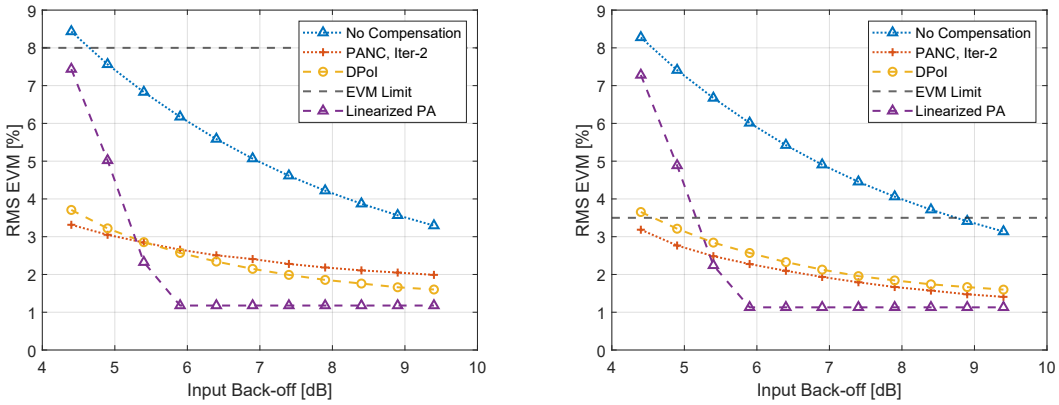

(a) *64QAM* ***(b)*** *256QAM*

Figure 4.6. *EVM simulation results for TDL-E channel with 50 ns RMS delay spread, memoryless PA. Parameter estimation is performed with noisy signal whereas EVM values are calculated from noiseless signal.*

Next, Figures 4.5-4.6 shows the simulation results for TDL-E channel with 30 ns and 50 ns RMS delay spreads. It can be observed that in the case of multipath channel, both methods exhibit similar performance to AWGN-only channel case.

4.2.2 Power Amplifier with Memory

Memory polynomial model is again used to represent the power amplifier with nonlinearity order of 11 and memory depth of 2. The nonlinear complex coefficients in this case is given in Table 4.4. AM/AM responses of the considered PA and the corresponding ideally linearized PA are illustrated in Figure 4.3b.

Figures 4.7a and 4.7b shows the EVM results for PA with memory effects under AWGN

Table 4.4. *Coefficients of PA model with memory*

Coefficient	Value	Coefficient	Value	Coefficient	Value
$c_{1,0}$	$0.9133 - j0.2230$	$c_{1,1}$	$0.4580 + j0.4978$	$c_{1,2}$	$-0.2460 - j0.3948$
$c_{3,0}$	$-0.0957 + j0.0956$	$c_{3,1}$	$0.0131 - j0.0034$	$c_{3,2}$	$-0.0058 + j0.0009$
$c_{5,0}$	$0.0302 + j0.0004$	$c_{5,1}$	$(5.2361 + j7.0282) \times 10^{-4}$	$c_{5,2}$	$(7.6286 + j5.9575) \times 10^{-4}$
$c_{7,0}$	$-0.0201 - j0.0183$	$c_{7,1}$	$-0.0039 - j0.0022$	$c_{7,2}$	$(8.5494 - j0.0871) \times 10^{-4}$
$c_{9,0}$	$0.0050 + j0.0049$	$c_{9,1}$	$0.0011 + j0.0009$	$c_{9,2}$	$(-2.4278 - j0.6766) \times 10^{-4}$
$c_{11,0}$	$(-3.9959 - j3.8728) \times 10^{-4}$	$c_{11,1}$	$(-9.4805 - j8.4753) \times 10^{-5}$	$c_{11,2}$	$(-1.8881 + j0.8612) \times 10^{-5}$

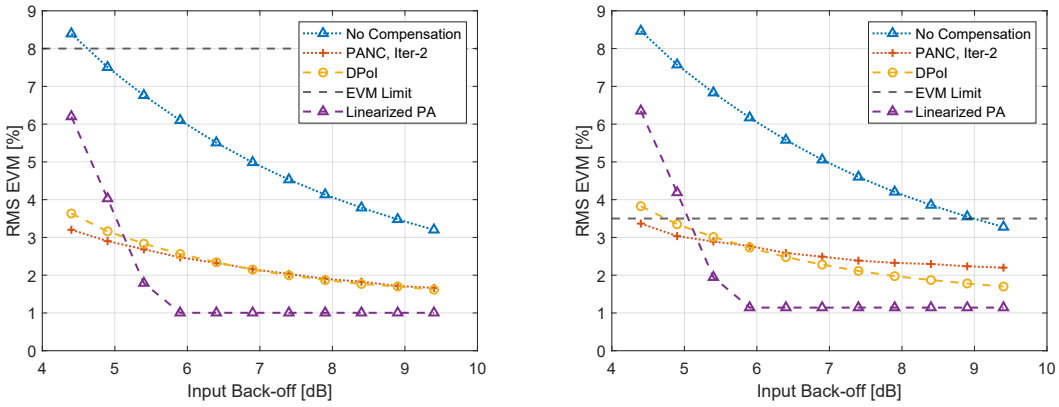

(a) *64QAM* ***(b)*** *256QAM*

Figure 4.7. *EVM simulation results for AWGN-only channel, PA with memory effects. Parameter estimation is performed with noisy signal whereas EVM values are calculated from noiseless signal.*

channel for 64QAM and 256QAM, respectively. There is no notable difference in performance when compared to corresponding memoryless cases.

Figures 4.8-4.9 show that both methods are providing significant improvement in terms of receiver EVM performance, even with memory effects and multipath scattering is present in the system.

4.2.3 Computational Complexity Analysis

Next, the computational complexities of the reference PANC and proposed DPoI method are presented in terms of real multiplications and real additions, denoted as $O(.) = (muls, adds)$. Contribution of receiver side operations such as channel estimation and LMMSE equalization to the computational complexity is omitted as they are common in both cases and performed anyway irrespective of the presence of post-distortion methods. It is assumed that FFT/IFFT operations are performed with radix-2 Cooley-Tukey algorithm [37]. Furthermore, we assume that basis functions can be generated in a recursive manner using previous basis functions for orders greater than 3, such that

$$\Upsilon_{(p+1),d} = \Upsilon_{p,d}|q(n)|^2, \quad p \geq 3. \tag{4.5}$$

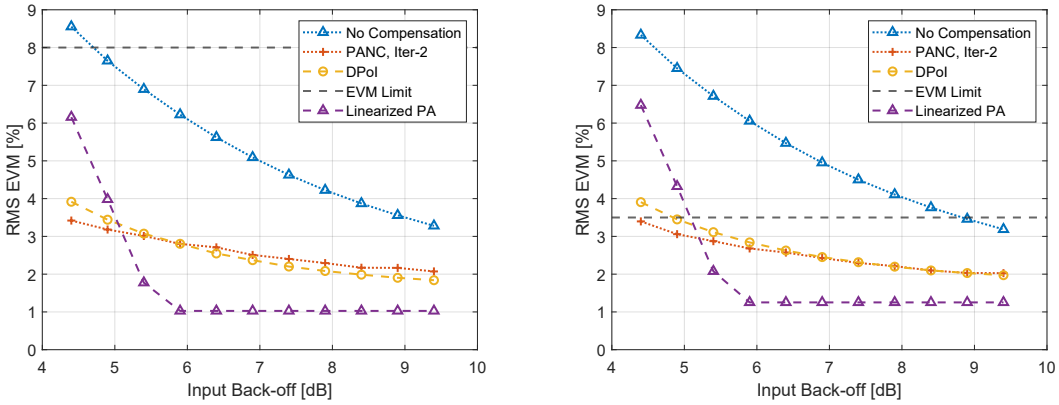

(a) *64QAM* ***(b)*** *256QAM*

Figure 4.8. *EVM simulation results for TDL-E channel with 30 ns RMS delay spread, PA with memory effects. Parameter estimation is performed with noisy signal whereas EVM values are calculated from noiseless signal.*

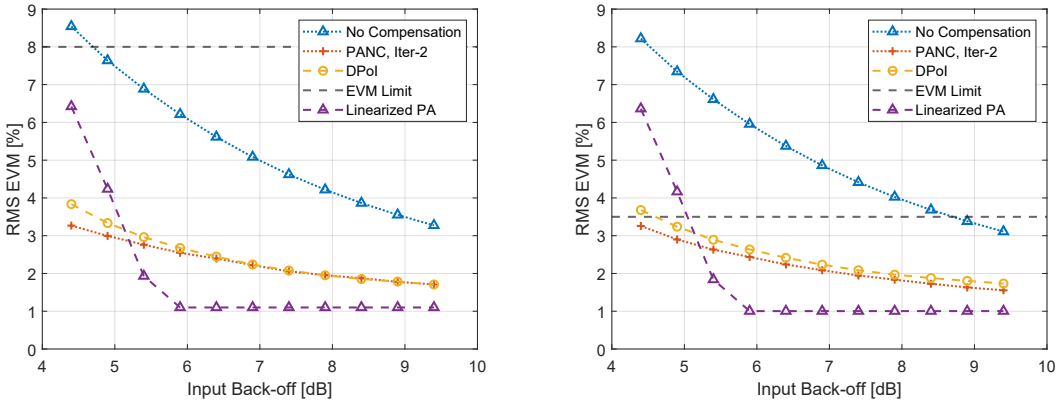

(a) *64QAM* ***(b)*** *256QAM*

Figure 4.9. *EVM simulation results for TDL-E channel with 50 ns RMS delay spread, PA with memory effects. Parameter estimation is performed with noisy signal whereas EVM values are calculated from noiseless signal.*

Basis functions with memory can be simply generated by sample shifting without requiring any multiplications and additions. Also, nonlinear parameter estimation, either forward or inverse, is common to both methods, thus it is not taken into account in computational complexity analysis.

For a system with N-point FFT/IFFT operation, M-QAM modulation, nonlinearity order of P and memory depth of D, computational complexity of PANC can be derived as follows: The first step of PANC algorithm is transforming equalized modulation symbols back to time domain via N-point FFT/IFFT operation which requires

$$O(\text{FFT/IFFT}) = (8Nlog_2N, 6Nlog_2N). \tag{4.6}$$

The next step is generating nonlinear output estimate through memory polynomial model, which can be represented in vector-matrix notation as

$$\boldsymbol{y} = \boldsymbol{\Upsilon}\boldsymbol{c}, \tag{4.7}$$

where $\boldsymbol{\Upsilon}$ is $N \times N_c$ basis function matrix constructed with the receiver-side estimate of PA input, $\boldsymbol{c}$ is $N_c \times 1$ nonlinear coefficient vector, and $N_c = (P_{\text{RX}} + 1)(D_{\text{RX}} + 1)/2$. The computational cost of executing 4.7 including the generation of basis function matrix is equal to

$$O(\text{MP}) = (4NN_c + N(P_{\text{RX}} + 1), N(4N_c - 1)). \tag{4.8}$$

The time domain distortion term is calculated simply as $d(n) = \tilde{y}(n) - \tilde{x}(n)$, where $\tilde{x}(n)$ and $\tilde{y}(n)$ are receiver-side estimates of PA input and output signals, respectively, and results in a complexity of

$$O(d(n)) = (0, 2N). \tag{4.9}$$

Next, frequency domain distortion term is obtained via N-point FFT operation, resulting in a complexity of $O(\text{FFT/IFFT}) = (8Nlog_2N, 6Nlog_2N)$. The last step of a single iteration of PANC is decoding, which we assume hard decoding is employed, has a complexity of $O(\text{Hard Decoding}) = (2MN_{\text{act}}, 3MN_{\text{act}})$, where M is the modulation order and N_{act} is the number of active subcarriers.

As a result, a single iteration of PANC requires

$$O_i(\text{PANC}) = \begin{matrix} 16Nlog_2N + 4NN_c + N(P_{\text{RX}} + 1) + 2MN_{\text{act}}\ muls \\ 12Nlog_2N + N(4N_c - 1) + 2N + 3MN_{\text{act}}\ adds. \end{matrix} \tag{4.10}$$

Overall computational complexity of PANC can be simply calculated by multiplying 4.10 with the number of iterations, i.e.

$$O(\text{PANC}) = n_{iter}O_i(\text{PANC}). \tag{4.11}$$

The computational complexity of DPoI method is consisted of only FFT/IFFT operation and MP execution, and can be expressed as

$$O(\text{DPoI}) = \begin{matrix} 16Nlog_2N + 4NN_c + N(P_{\text{RX}} + 1)\ muls \\ 12Nlog_2N + N(4N_c - 1)\ adds. \end{matrix} \tag{4.12}$$

As a numerical example, substituting the values used in the simulations, i.e. $N = \varepsilon N_{\text{FFT}} = 5 \times 4096 = 20480$, $N_{\text{act}} = 3168$, $P_{\text{RX}} = 7$, $D_{\text{RX}} = 4$, $M = 64$ or $M = 256$, and $n_iter = 2$ for PANC, yields a computational complexity of

$$O(\text{PANC}) = \begin{cases} (9.8949 \times 10^6, 8.6439 \times 10^6) & M = 64 \\ (1.2328 \times 10^7, 1.2293 \times 10^7) & M = 256 \end{cases} \tag{4.13}$$
$$O(\text{DPoI}) = (4.5620 \times 10^6, 3.6727 \times 10^6),$$

that shows that the computational cost of DPoI is less than half of the computational cost of PANC and also implies that computational complexity of PANC increases with increasing number of iterations and modulation order, whereas computational complexity of DPoI does not depend on the modulation order.

5. CONCLUSIONS

DPD is widely used and can be considered as the de-facto solution to migitage the PA nonlinear distortion in modern wireless communications, however, future mmWave systems with wide bandwidths and active antenna arrays result in an increased complexity and cost for DPD implementation. Receiver side digital post-distortion techniques can be considered as a promising solution to this problem and a computationally efficient digital post-distortion technique was presented and studied in this thesis.

Compared to the existing iterative DPoD methods, the proposed DPoI method is a one-shot approach which makes it computationally efficient. Furthermore, it does not require any *a priori* knowledge of transmitter nonlinear characteristics, and consists an inverse nonlinear model parameter estimation and corresponding nonlinear post-inverse processing. In general, parameter estimation can be done on any reference signal that has an envelope characteristics matching with envelope characteristics of the signal to be post-distorted, however, in this thesis, proposed approach is analyzed assuming a 5G NR SISO downlink transmission and parameter estimation is built on an existing standard-compliant reference signal, namely DM-RS. With the assumption of subcarriers carrying non-DM-RS modulation symbols are forced to be zero in a DM-RS OFDM symbol, a boosting approach is proposed to have a matching envelope characteristics for the reference signal and the signal to be post-distorted.

A set of simulations were carried out to verify the performance of digital post-distortion methods. PANC method was used as a reference DPoD method. Also, both PANC and DPoI methods were compared to ideally linearized transmitter PA. Power amplifiers with and without memory effects were analyzed separately, under a multipath channel propagation with varying RMS delay spread and a constant AWGN of 20 dB SNR. A set of simulations were performed for modulation schemes of 64QAM and 256QAM. Receiver EVM was used as a performance comparison metric, which is calculated using a noiseless signal whereas parameter estimation is performed using a noisy signal.

Simulation results showed that both DPoD methods provide significant improvement in terms of receiver EVM, ensuring EVM requirements specified in [36] are fulfilled in each case. Proposed DPoI approach showed a similar performance compared to PANC method, but with greatly reduced computational complexity. These findings were further

assessed and confirmed through actual RF measurements at 28 GHz in [8], stemming directly from this thesis work. It should be also noted that the computational complexity of PANC increases with increasing modulation order, whereas the computational complexity of DPoI does not depend on modulation order, which is especially important when future mmWave networks are considered. Furthermore, due to its limited linear operation range, considered ideally linearized PA requires a certain input back-off applied to input signal when the input signal has a high PAPR. Both DPoD methods, on the other hand, overperformed ideally linearized PA under strong nonlinear conditions, allowing PA to be pushed further into its nonlinear region which results in an increased efficiency and improved cell coverage. Such substantial energy-efficiency benefits are likely to play a key role in future 6G networks where the overall sustainability requirements are expected to be further boosted compared to the current 5G systems.

REFERENCES

[1] F. Gregorio, G. González, C. Schmidt, and J. Cousseau, *Signal Processing Techniques for Power Efficient Wireless Communication Systems, Practical Approaches for RF Impairments Reduction*. Jan. 2020. DOI: 10.1007/978-3-030-32437-7.

[2] J. Wood, *Behavioral modeling and linearization of RF power amplifiers* (Artech House microwave library). Artech House, 2014.

[3] C. Fager, T. Eriksson, F. Barradas, K. Hausmair, T. Cunha, and J. C. Pedro, "Linearity and efficiency in 5G transmitters: New techniques for analyzing efficiency, linearity, and linearization in a 5g active antenna transmitter context," *IEEE Microwave Magazine*, vol. 20, no. 5, pp. 35–49, 2019. DOI: 10.1109/MMM.2019.2898020.

[4] L. Guan and A. Zhu, "Green communications: Digital predistortion for wideband RF power amplifiers," *IEEE Microwave Magazine*, vol. 15, no. 7, pp. 84–99, 2014. DOI: 10.1109/MMM.2014.2356037.

[5] Z. Alina and O. Amrani, "On digital post-distortion techniques," *IEEE Transactions on Signal Processing*, vol. 64, no. 3, pp. 603–614, 2016. DOI: 10.1109/TSP.2015.2477806.

[6] A. Brihuega, M. Abdelaziz, L. Anttila, *et al.*, "Piecewise digital predistortion for mmwave active antenna arrays: Algorithms and measurements," *IEEE Transactions on Microwave Theory and Techniques*, vol. 68, no. 9, pp. 4000–4017, 2020. DOI: 10.1109/TMTT.2020.2994311.

[7] J. Tellado, L. Hoo, and J. Cioffi, "Maximum-likelihood detection of nonlinearly distorted multicarrier symbols by iterative decoding," *IEEE Transactions on Communications*, vol. 51, no. 2, pp. 218–228, 2003. DOI: 10.1109/TCOMM.2003.809289.

[8] H. Babaroglu, L. Anttila, G. Xu, M. Turunen, M. Allén, and M. Valkama, "Cellular digital post-distortion: Signal processing methods and RF measurements," in *2023 IEEE 23rd Annual Wireless and Microwave Technology Conference (WAMICON)*, 2023.

[9] R. W. Chang, "Synthesis of band-limited orthogonal signals for multichannel data transmission," *The Bell System Technical Journal*, vol. 45, no. 10, pp. 1775–1796, 1966. DOI: 10.1002/j.1538-7305.1966.tb02435.x.

[10] 3GPP, "Physical channels and modulation (Release 16)," Technical Specification (TS) 38.211, June 2022, Version 16.10.0.

[11] E. Dahlman, S. Parkvall, and J. Sköld, *5G NR : the next generation wireless access technology*, Second edition. Academic Press, an imprint of Elsevier, 2021.

[12] C. Cox, *Introduction to 5G - The New Radio, 5G Network and Beyond*. John Wiley and Sons, 2021.

[13] 3GPP, “Base Station (BS) radio transmission and reception (Release 16),” Technical Specification (TS) 38.104, Dec. 2022, Version 16.14.0.

[14] A. Goldsmith, *Wireless Communications*. Cambridge University Press, 2005.

[15] T. Jiang, M. Guizani, H.-H. Chen, W. Xiang, and Y. Wu, “Derivation of papr distribution for ofdm wireless systems based on extreme value theory,” *IEEE Transactions on Wireless Communications*, vol. 7, no. 4, pp. 1298–1305, 2008. DOI: 10.1109/TWC.2008.060862.

[16] M. Almalkawi, *RF and Microwave Module Level Design and Integration*. Institution of Engineering and Technology (The IET), 2019.

[17] H. Wang and K. Sengupta, *RF and mm-Wave Power Generation in Silicon*. Elsevier, 2016.

[18] K. Chang, *Encyclopedia of RF and Microwave Engineering, Volumes 1 - 6*. Wiley, 2005.

[19] D. Del Corso, V. Camarchia, and R. Quaglia, *Telecommunication Electronics*. Artech House, 2020.

[20] D. M. Pozar, *Microwave engineering*, 4th ed. Wiley, 2012.

[21] A. Moulthrop, C. Clark, C. Silva, and M. Muha, “A dynamic AM/AM and AM/PM measurement technique,” in *1997 IEEE MTT-S International Microwave Symposium Digest*, vol. 3, 1997, 1455–1458 vol.3.

[22] C. Clark, C. Silva, A. Moulthrop, and M. Muha, “Power-amplifier characterization using a two-tone measurement technique,” *IEEE Transactions on Microwave Theory and Techniques*, vol. 50, no. 6, pp. 1590–1602, 2002. DOI: 10.1109/TMTT.2002.1006421.

[23] J. Pedro and S. Maas, “A comparative overview of microwave and wireless power-amplifier behavioral modeling approaches,” *IEEE Transactions on Microwave Theory and Techniques*, vol. 53, no. 4, pp. 1150–1163, 2005. DOI: 10.1109/TMTT.2005.845723.

[24] D. Schreurs, M. O’Droma, A. Goacher, and M. Gadringer, *RF Power Amplifier Behavioral Modeling* (The Cambridge RF and Microwave Engineering Series), 1st ed. Cambridge University Press, 2008.

[25] A. Saleh, “Frequency-independent and frequency-dependent nonlinear models of TWT amplifiers,” *IEEE Transactions on Communications*, vol. 29, no. 11, pp. 1715–1720, 1981. DOI: 10.1109/TCOM.1981.1094911.

[26] V. Mathews and G. Sicuranza, *Polynomial Signal Processing* (Wiley Series in Telecommunications and Signal Processing). Wiley, 2000.

[27] G. Montoro and P. L. Gilabert, “Power amplifier nonlinear modeling for digital predistortion,” in *Digital Front-End in Wireless Communications and Broadcasting: Cir-*

cuits and Signal Processing, F.-L. Luo, Ed. Cambridge University Press, 2011, pp. 192–213. DOI: 10.1017/CBO9780511744839.008.

[28] L. Ding, G. Zhou, D. Morgan, *et al.*, "A robust digital baseband predistorter constructed using memory polynomials," *IEEE Transactions on Communications*, vol. 52, no. 1, pp. 159–165, 2004. DOI: 10.1109/TCOMM.2003.822188.

[29] D. Morgan, Z. Ma, J. Kim, M. Zierdt, and J. Pastalan, "A generalized memory polynomial model for digital predistortion of RF power amplifiers," *IEEE Transactions on Signal Processing*, vol. 54, no. 10, pp. 3852–3860, 2006. DOI: 10.1109/TSP.2006.879264.

[30] A. Katz, J. Wood, and D. Chokola, "The evolution of PA linearization: From classic feedforward and feedback through analog and digital predistortion," *IEEE Microwave Magazine*, vol. 17, no. 2, pp. 32–40, 2016. DOI: 10.1109/MMM.2015.2498079.

[31] J. Šterba, J. Gazda, M. Deumal, and D. Kocur, "Iterative algorithm for nonlinear noise cancellation and channel re-estimation in nonlinearly distorted OFDM system," in *2010 IEEE 8th International Symposium on Applied Machine Intelligence and Informatics (SAMI)*, 2010, pp. 65–70. DOI: 10.1109/SAMI.2010.5423768.

[32] F. Gregorio, S. Werner, T. I. Laakso, and J. Cousseau, "Receiver cancellation technique for nonlinear power amplifier distortion in SDMA–OFDM systems," *IEEE Transactions on Vehicular Technology*, vol. 56, no. 5, pp. 2499–2516, 2007. DOI: 10.1109/TVT.2007.899965.

[33] F. H. Gregorio, S. Werner, J. E. Cousseau, and R. Wichman, "Broadband power amplifier distortion cancellation with model estimation in the receiver," in *2007 IEEE 8th Workshop on Signal Processing Advances in Wireless Communications*, 2007, pp. 1–5. DOI: 10.1109/SPAWC.2007.4401407.

[34] D. Morgan, Z. Ma, and L. Ding, "Reducing measurement noise effects in digital predistortion of RF power amplifiers," in *IEEE International Conference on Communications, 2003. ICC '03.*, vol. 4, 2003, 2436–2439 vol.4. DOI: 10.1109/ICC.2003.1204371.

[35] 3GPP, "Study on channel model for frequencies from 0.5 to 100 GHz (Release 16)," Technical Report (TR) 38.901, Dec. 2019, Version 16.1.0.

[36] 3GPP, "User Equipment (UE) conformance specification; Radio transmission and reception; Part 1: Range 1 standalone (Release 16)," Technical Specification (TS) 38.521-1, June 2019, Version 16.8.0.

[37] J. W. Cooley and J. W. Tukey, "An algorithm for the machine calculation of complex Fourier series," *Mathematics of Computation*, vol. 19, pp. 297–301, 1965.